Electron cryo-microscopy structure of the canonical TRPC4 ion channel

Deivanayagabarathy Vinayagam[1], Thomas Mager[2], Amir Apelbaum[1], Arne Bothe[1], Felipe Merino[1], Oliver Hofnagel[1], Christos Gatsogiannis[1], Stefan Raunser[1]

[1]Department of Structural Biochemistry, Max Planck Institute of Molecular Physiology, 44227 Dortmund, Germany

[2]Department of Biophysical Chemistry, Max Planck Institute of Biophysics, 60438 Frankfurt am Main, Germany

Correspondence: stefan.raunser@mpi-dortmund.mpg.de

ABSTRACT

Canonical transient receptor channels (TRPC) are non-selective cation channels. They are involved in receptor-operated Ca^{2+} signaling and have been proposed to act as store-operated channels (SOC). Their malfunction is related to cardiomyopathies and their modulation by small molecules has been shown to be effective against renal cancer cells. The molecular mechanism underlying the complex activation and regulation is poorly understood. Here, we report the electron cryo-microscopy structure of zebrafish TRPC4 in its unliganded (apo), closed state at an overall resolution of 3.6 Å. The structure reveals the molecular architecture of the cation conducting pore, including the selectivity filter and lower gate. The cytoplasmic domain contains two key hubs that have been shown to interact with modulating proteins. Structural comparisons with other TRP channels give novel insights into the general architecture and domain organization of this superfamily of channels and help to understand their function and pharmacology.

1

INTRODUCTION

Transient receptor potential (TRP) channels constitute a large superfamily of ion channels that can be grouped in seven subfamilies: TRPC, TRPM, TRPML, TRPP, TRPV, TRPA and TRPN (Montell, 2005). The channels of the TRP superfamily are diverse in respect to modes of activities, ion selectivity and physiological functions. Most TRP channels are non-selective cation channels with varying preferences for Ca^{2+} over Na^+ (Owsianik et al., 2006). Some TRPs are physically stimulated or voltage-activated, whereas others respond to the binding of ligands or the direct interaction with other proteins. Corresponding to their functional diversity TRPs are involved in many cellular processes, including mechanosensation, thermosensitivity, nociception and store-operated Ca^{2+} entry (Nilius and Flockerzi, 2014).

TRPC4 is one of seven members of the subfamily of TRPC (canonical TRPs) channels (Freichel et al., 2014). TRPC channels are Ca^{2+}/Na^+-permeable cation channels that are expressed in many cell types and tissues, including brain, placenta, adrenal gland, retina endothelia, testis, and kidney (Freichel et al., 2014). The channels play an important role in vasorelaxation and neurotransmitter release. TRPC4 contributes to axonal regeneration after nerve injury (Wu et al., 2008) and TRPC channels in general are necessary mediators of pathologic cardiac hypertrophy (Wu et al., 2010).

The activation mechanism of TRPC4 has been controversially discussed (Plant and Schaefer, 2003). Dependent on the cellular environment and method of measurement, the reported activation mechanism, permeability and biophysical properties differ for TRPC4 and its close homologue TRPC5 (Plant and Schaefer, 2003). Several studies showed that TRPC4 and TRPC5 form receptor-operated, Ca^{2+}-permeable, non-selective cation channels (Okada et al., 1998; Schaefer et al., 2000). Others found that TRPC4 and TRPC5 are activated by Ca^{2+} store-depletion with moderate to high Ca^{2+} permeabilities (Philipp et al., 1996; Warnat et al., 1999). In line with both findings, TRPC4 directly interacts with IP_3 receptors, calmodulin (Mery et al., 2001; Tang et al., 2001), STIM1 (Lee et al., 2010; Zeng et al., 2008), the lipid-binding protein SESTD1 (Miehe et al., 2010) and the G protein $G_{\alpha i2}$ (Jeon et al., 2012). SESTD1 binds several phospholipid species and is essential for efficient receptor-mediated activation of TRPC5 (Miehe et al., 2010). In addition, TRPC channels have been shown to be activated by NO (Yoshida et al., 2006).

Recently, (-)-Englerin A has been shown to be a potent and selective activator of TRPC4 and TRPC5 calcium channels (Akbulut et al., 2015). It selectively kills renal cancer cells by elevated Ca^{2+} influx. (-)-Englerin A is so far the only known potent activator of TRPC4 and TRPC5.

2

The resolution revolution in cryo-EM (Kühlbrandt, 2014) brought an enormous amount of high-resolution structures of TRP channels in the last 5 years (Madej and Ziegler, 2018). The cryo-EM structure of TRPV1 (Liao et al., 2013) ushered structural biology of TRP channels in a new era. So far structure models for 48 TRP channels from 6 subfamilies have been published (Madej and Ziegler, 2018). The TRPCs represent the only subfamily for which no high-resolution structure has been reported so far limiting our understanding of these important type of cation channels. Here, we present the first cryo-EM structure of zebrafish TRPC4 in its unliganded (apo), closed state.

RESULTS & DISCUSSION

Initially, we planned to heterologously express human TRPC4 in HEK293 cells and purify it to determine its structure by single particle cryo-EM. However, the protein proved not to be stable enough for structural investigations. We therefore screened TRPC4 orthologues from several different species and found wild type TRPC4 from zebrafish (TRPC4$_{DR}$) to be the most suitable for our studies. TRPC4$_{DR}$ has very high sequence similarity to human TRPC4 (76 % sequence identity, Figure S1).

To determine whether TRPC4$_{DR}$ has the same channel properties as human TRPC4, we performed voltage-clamp experiments with HEK293 cells heterologously expressing TRPC4$_{DR}$. The measurements demonstrated that, like human TRPC4 (Akbulut et al., 2015), TRPC4$_{DR}$ can be activated by (-)-Englerin A resulting in similar currents (Figure 1a-b). Of note, current-voltage curves (IV-curves) in the presence of (-)-Englerin A showed a doubly rectifying form (Figure 1c) and reversal potentials close to 0 mV (-3.2 ± 1.7 mV, n=6). The doubly rectifying form of the IV-curve is a characteristic hallmark of active TRPC4 (Akbulut et al., 2015; Freichel et al., 2014; Schaefer et al., 2000). Under the experimental conditions, namely asymmetric ion concentrations, reversal potentials close to 0 mV indicate a poor cation selectivity, which is a known property of several TRPC4 variants from different species (Freichel et al., 2014; Schaefer et al., 2002).

We overexpressed Strep-tagged TRPC4$_{DR}$ in HEK293, solubilized it in n-dodecyl-β-d-maltopyranoside (DDM)/cholesteryl hemisuccinate (CHS) and purified it using affinity and size exclusion chromatography (Figure S2a-b). After purification the detergent was exchanged against amphipols. The resulting sample was homogeneous and suitable for structural studies (see Methods, Figure S2c-e). We then solved the structure of TRPC4$_{DR}$ in its unliganded (apo), closed state by cryo-EM and single-particle analysis (see Methods) at an average resolution of

3.6 Å (Figure 2a, Table S1, Figure S3-4, Movie S1). The high quality of the map allowed us to build a model of 70 % of TRPC4$_{DR}$ *de novo*. The final model contains residues 18-753 with some loops missing (Figure 2b). As in most other TRP structures the C-terminal region (residues 754-915) could not be resolved indicating that this region is highly flexible.

The overall structure of the homotetrameric TRPC4$_{DR}$ is similar that of other TRP channels (Figure 2a-b). Especially the transmembrane domain comprising the voltage-sensor-like (VSL) domain and pore domain is structurally conserved. Like TRPVs, TRPMs, TRPAs and TRPNs, TRPC4$_{DR}$ does not have extracellular but extended cytoplasmic domains. The resolved regions of the cytoplasmic domain of TRPC4$_{DR}$ reaches ~ 80 Å into the cytosol and is relatively short compared to other TRP channels. The cytoplasmic domain can be separated in an upper and lower part. The upper part comprises a conserved TRP domain, a pre-S1 elbow domain that enters partially the membrane and an extended helical linker domain (Figure 2c-d). The lower part is formed by the Rib (or Stretcher) helix, the C-terminal helix and four ankyrin repeats (Figure 2c-d). 3-D classification and refinement of the final data set (Figure S4) revealed that the lower cytoplasmic part of TRPC4$_{DR}$ is flexible, whereas the transmembrane domain is not (Movie S2).

Voltage-sensor like domain and ion conducting pore

Although TRP channels are only mildly voltage-sensitive, they contain a structurally conserved VSL domain comprising four helices (S1-S4). Helix S4 harbors the key residues involved in voltage sensing in voltage-gated ion channels (Swartz, 2008). Comparing helix S4 in our structure with that one in the structure of the Kv1.2-Kv2.1 paddle chimera (Long et al., 2007), we found that R491 in TRPC4$_{DR}$ is located at the same position as R302 in the potassium channel (Figure 3a). An arginine at this position is also observed in TRPM4 and TRPM8, which possess weak voltage dependency (Winkler et al., 2017; Yin et al., 2018), but not in TRPV1 (Gao et al., 2016; Liao et al., 2013) (Figure 3a). Other positively charged residues that are involved in voltage sensing in Kv1.2, such as R293, R296, R299, R302, R305, and K308 are replaced by polar residues, including N485, S488, S494, and T497 in TRPC4$_{DR}$. This is in sharp contrast to TRPM4 and TRPV1 channels in which the VSL domain comprises mostly hydrophobic residues (Liao et al., 2013; Winkler et al., 2017) (Figure 3a). Hence, based on the structure of TRPC4$_{DR}$ TRPC channels could exhibit a certain level of voltage sensitivity.

Upstream of the VSL domain resides the pre-S1 elbow domain. It sits inside the membrane and forms a cavity with helices S1 and S4 in which we could identify density corresponding to a CHS molecule (Figure 3b-c). Interestingly, a CHS molecule has also been

found at the same position in the structures of TRPM4 (Autzen et al., 2018) and TRPML3 (Hirschi et al., 2017). In a second cavity between the pre-S1 elbow domain and helices S1 and S2 resides a proline-rich repeat connecting the TRP and helical linker domains (see below).

The activation of TRPC4 and TRPC5 is dependent on Ca^{2+} (Plant and Schaefer, 2003). However, so far no Ca^{2+} binding sites have been described for TRPCs and we do not have Ca^{2+} in our sample buffer. Interestingly, the four coordinating residues that have been reported for binding of Ca^{2+} in Ca^{2+}-activated TRPM4 (Autzen et al., 2018) are conserved in TRPC4 (Figure S5). In the $TRPC4_{DR}$ structure, their position is very similar to TRPM4 and would allow the coordination of a Ca^{2+} ion (Figure S5).

Like in other TRP channels, helix S5 and S6 swap over to the respective helices of the adjacent protomer and form the pore at the center of the tetrameric channel (Figure 2b). The extracellular opening of the pore is negatively charged (Figure 4a) and the conserved residue E555 at the tip of the pore turret forms a salt bridge with R556 of the adjacent protomer (Figure S6a-b). This results in a positioning of E555 away from the pore and in a relatively wide opening of its entrance similar to TRPV1 (Liao et al., 2013) (Figure 4b-d). This is in contrast to the narrow pore openings of the more selective Ca^{2+} channels TRPV5 (Hughes et al., 2018) and TRPV6 (McGoldrick et al., 2018) and possibly explains the lower selectivity of TRPC4 channels. Mutation of E555 (E559 in TRPC1) to lysine results in decreased store-operated Ca^{2+} influx (Liu et al., 2003), suggesting that a negatively charged and stable pore opening is crucial for the undisturbed gating of cations through TRPCs.

The selectivity filter is formed by four glycine residues (G577) that constrict the pore to a diameter of 7.0 Å (3.7 Å defined by opposing van der Waals surfaces) (Figure 4c-d). Since the diameters of Na^+ and Ca^{2+} ions are ~ 2 Å in their dehydrated and ~ 10-12 Å in their fully hydrated state, the cations are likely partly dehydrated when passing through the selectivity filter. Although TRPs differ in their cation selectivity, there is no clear factor recognizable that determines the level of selectivity (Table 1). Neither the diameter of the filter, ranging from 1.8 to 8.4 Å, nor the type of residue, mostly glycine or aspartate, correlates with the selectivity of the channels for Na^+ or Ca^{2+} (Table 1). The level of selectivity must therefore be defined differently.

The lumen of the pore below the selectivity filter is mainly hydrophobic (Figure 4b) and leads to the lower gate at the cytoplasmic end formed the by the conserved residues I617 and N621 (Figure 4c). I617 belongs to the M3 motif found in all TRPCs, TRPVs, and TRPMs (Freichel et al., 2014). In our case, the $TRPC4_{DR}$ channel is almost completely closed. The four isoleucines and four asparagines constrict the pore to a diameter of ~ 5.3 Å and ~ 4.2 Å,

respectively (1.6 Å and 0.7 Å defined by opposing van der Waals surfaces) (Figure 4c-d). Ca^{2+} and Na^+ ions are too large to fit through these constrictions even in a dehydrated state. The lower constriction of the TRPP channel PKD2 is also formed by an asparagine and leads to a closure of the pore (Shen et al., 2016a).

An important region inside the pore domain is the LFW motif (residues 571-573), which is also conserved in TRPC1 and TRPC5. In TRPC5, mutation of the LFW motif to AAA results in non-functional but folded channels (Strübing et al., 2003). In our TrpC4$_{DR}$ structure F572 and W573 form part of a prominent hydrophobic contact between the pore helix of one protomer and helix S6 of the adjacent protomer, stabilizing the pore (Figure S6c-d). The triple AAA mutation in this region likely destabilizes this interaction and results in the collapse of the pore explaining the inactivity of the channel. Interestingly, we found an additional density corresponding to a phosphatidic acid annular lipid at this interface. The phosphate head group interacts with T599 of helix S6 and W573 and Q569 of the pore helix (Figure 3b). The non-polar tail group is stabilized by interaction with multiple hydrophobic residues from the surrounding helices S5, S6 and the pore helix (Figure 3d).

Another well-studied region of the pore domain contains two cysteines (C549 and C554). Yoshida et al. showed that S-nitrosylation of these residues in TRPC5 leads to the activation of the channel (Yoshida et al., 2006). The authors proposed that the modification of the residues has a direct effect on the conformation of helix S6, resulting in the opening of the gate. In the TRPC4 structure, however, C549 and C554 do not locate in close proximity to helix S6 (Figure S6a-b). We can therefore exclude a direct interaction. In agreement with the structure of TRPM4 in the calcium-free state (Autzen et al., 2018), these residues form a disulfide bridge in TRPC4$_{DR}$ (Figure S6a-b). In TRPM4, this has an overall effect on the upper part of the channel, but does not influence the selectivity filter. In our case, however, the cysteines are likely involved in putting E555 in place, which forms the upper site of selectivity filter (see above). Nitrosylation in the presence of Ca^{2+}, when the cysteines are reduced (Autzen et al., 2018), could lead to a destabilization of the upper region of the selectivity filter, altering its properties. In addition, the conformational change could result in a negatively charged sink at the turret, thereby attracting cations, explaining the effect of the increased Ca^{2+} conductance observed by Yoshida et al. (Yoshida et al., 2006).

The TRP domain and helical linker domain

The TRP domain and linker domain connect the transmembrane domain with the lower cytoplasmic domain (Figure 2c-d). The TRP domain (residues E634 – N658) resides directly

6

after helix S6 and is sandwiched between the linker and transmembrane domains. It is conserved in all TRP subfamilies except TRPPs and TRPMLs (Madej and Ziegler, 2018; Venkatachalam and Montell, 2007). The core of the TRP domain consists of the conserved WKXQR TRP box sequence (residues 635-639). Its central residue W635 has been shown to be of crucial importance for gating of several TRP channels. Its mutation in TRPV3 leads to Olmsted syndrome (Lin et al., 2012) and in NOMPC an exchange to alanine results in a channel with a prominent basal current that does not respond to mechanical stimuli anymore (Jin et al., 2017a).

Like in other TRP domain-containing TRPs, W635 in TRPC4$_{DR}$ interacts with the conserved G503 in the adjacent M2 motif (residues 502-511) thereby linking the TRP domain with the linker between helices S4-S5 (Figure 5a-b). G503 is conserved in all TRP subfamilies containing a TRP domain (Figure 5c). Mutation of this residue to serine in TRPC4 and TRPC5 forces the channels in an open conformation (Beck et al., 2013). The proper interaction between G503 and W635 guarantees the stabilization of helix S6 that forms the lower gate of the pore. It becomes clear from looking at these residues in our TRPC4$_{DR}$ structure, that a G503S or W635A mutation would impair the interaction at this site and result in the loss of control over the gate (Figure 5b).

E648 and E649 which are conserved in TRPC4 and TRPC5 (Figure S1) are located at a peripheral loop of the TRP domain. The glutamates interact electrostatically with two lysine residues (K684 and K685) in Stim1 proteins resulting in the activation of cation currents (Lee et al., 2010; Zeng et al., 2008). In line with this biochemical finding, E648 and E649 (E649 is not resolved in our structure) are exposed at the periphery of TRPC4$_{DR}$ and are accessible for interactions with other proteins.

TRPC4$_{DR}$ contains two conserved proline-rich regions downstream of the TRP domain. Proline-rich regions are often involved in specific protein-protein interactions and signal transmission. In TRPC4$_{DR}$ the first proline-rich region formed by P654, P655, P656 re-enters the membrane and is sandwiched between the pre-S1 elbow domain and helix S2 making it inaccessible from the cytoplasm or the membrane. The second proline-rich region around the residues P660 and P662 is not resolved in our structure but this region is located at the outside of the protein and could thereby be accessible for interacting with regulating proteins like Homer. Homer is an adaptor protein that facilitates the physical interaction between TRPC1 and the IP$_3$ receptor (Yuan et al., 2003).

The helical linker domain is made of three layers of helices that are arranged like stair steps and a coil of shorter helices (Figure 2d). The upper layer of helices harbors the M1 motif

(residues 285-319), which is conserved in the TRPC family (Flockerzi, 2007). The central two helices form a short coiled-coil structure that harbors the multimerization motif (residues D254 -Q302), that has been predicted to be involved in the multimerization of TRPCs (Freichel et al., 2014). Indeed, in contrast to other TRP family members (Madej and Ziegler, 2018), the helical linker domain does not only connect the transmembrane domain with the lower cytoplasmic domain but also strongly interacts with the adjacent linker domains thereby stabilizing the tetramer (Figure 2a-b). This kind of interaction has not been observed in the structures of other TRP subfamily members, such as TRPA1 (Paulsen et al., 2015), NOMPC (Jin et al., 2017b) and TRPM4 (Autzen et al., 2018; Guo et al., 2017; Winkler et al., 2017). In the TRPV subfamily the cytoplasmic inter-protomer interaction is mediated between the ankyrin repeat domain of one protomer and the β-strand linker domain of the adjacent protomer (Liao et al., 2013).

The lower part of the cytoplasmic domain

Ankyrin repeats, the Rib helix, and C-terminal helix domain constitute the most distant region of TRPC4$_{DR}$ (Figure 2c-d). Ankyrin repeats, that are often involved in protein-protein interactions (Sedgwick and Smerdon, 1999), are abundant in TRP channels in varying numbers, ranging from 0 in TRPP (Shen et al., 2016a) and TRPML (Chen et al., 2017; Hirschi et al., 2017; Schmiege et al., 2017; Zhou et al., 2017) to 29 in NOMPC (Jin et al., 2017b). In most structures of TRPs the first ankyrin repeats are oriented in a parallel fashion like in TRPA1 (Paulsen et al., 2015) (Figure 6a). TRPCs contain 4 ankyrin repeats in the cytoplasmic domain. Biochemical studies have shown that at least the first ankyrin repeat is necessary in TRPC5 for proper tetramerization and function of the channel (Schindl et al., 2008). In the structure of TRPC4$_{DR}$ the repeats take a unique twisted orientation and swap over to an adjacent protomer interacting with the C-terminal helix domain and Rib domain explaining the ankyrin repeat's stabilizing effect on the tetramer (Figure 2b, 6b).

The Rib helix runs almost parallel to the membrane and protrudes from the cytoplasmic domain (Figure 7a). It contains a dual calmodulin- and IP$_3$ receptor-binding site (CIRB) (Mery et al., 2001; Tang et al., 2001) and has been described as binding hub not only for these proteins but also for SESTD1 (Miehe et al., 2010) and the G protein G$_{\alpha i2}$ (Jeon et al., 2012) (Zhu, 2005). It is therefore a central interaction site for TRPC4-modulating proteins and the activity of the channel might be modulated by a displacement mechanism in which the different modulators compete for the same binding site (Zhu, 2005). A homologous helix has been observed in the structure of TRPM4 (Autzen et al., 2018; Guo et al., 2017; Winkler et al., 2017). However, in

the structure of TRPM4 the Rib helix is buried by other domains and only the very tip is accessible from the surface (Figure 7b). The Rib helix of TRPC4$_{DR}$, however, is accessible from the cytoplasm and direct binding of calmodulin or IP$_3$-receptor is possible (Figure S7).

A second major protein interaction hub is the C-terminal helix domain. It has only been observed before in TRPA1 (Paulsen et al., 2015), TRPM4 (Autzen et al., 2018; Guo et al., 2017; Winkler et al., 2017), and TRPM8 (Yin et al., 2018). In all described structures, it has a coiled-coil structure (Figure 8a-b). In the case of TRPC4$_{DR}$, however, the helices run in a parallel fashion (Figure 8c). The C-terminal helix domain has been shown to bind to the D$_2$ dopamine receptor (Hannan et al., 2008) and spectrin αII and βV which are involved in surface expression and activation of TRPC4 (Odell et al., 2008).

Our structure of TRPC4 misses 162 residues at the C-terminus. This part of the protein comprises a PDZ-binding domain (Mery et al., 2002) and a second IP$_3$-binding domain (Mery et al., 2001) and calmodulin binding sites (Tang et al., 2001; Trost et al., 2001). Interestingly, the largest part of this region is missing in the second most abundant splice variant of TRPC4, namely TRPC4β (Freichel et al., 2014). In line with our structural data, a sequence-based structure prediction indicates that this region has no defined secondary structure.

In summary, the results allow us to understand the three-dimensional organization of TRPC channels. The structure of TRPC4$_{DR}$ reveals how the gating pore is built and how cations are selected. Our results point towards a gating mechanism that is conserved in all TRP channels. Future studies will be needed to structurally understand how TRPCs are activated or in general modulated by proteins and other factors and gate cations. Our structure-based localization of previously biochemically identified protein binding sites provides the structural framework for further experiments towards understanding how binding of regulatory protein affect the structure and function of TRPC4.

Author contribution

S.R. designed the project. D.V., A.A., and A.B. optimized expression and purification of eukaryotic membrane proteins. D.V. expressed and purified TRPC4. O.H. recorded the EM images. D.V. prepared cryo-EM specimens, D.V. and C.G. processed cryo-EM data, and D.V. and F.M. built the atomic models. T.M. performed the electrophysiology experiments. D.V. and C.G. prepared figures and movies. S.R. wrote the manuscript with input from all authors. All authors reviewed the results and commented on the manuscript.

Declaration of interest

The authors declare no competing interest

Data availability

The atomic coordinates and cryo-EM maps for TRPC4$_{DR}$ are available at the PDB/EMDB databases. The accession numbers are XXXX/EMD-XXXX. The data sets generated in the current study are available from the corresponding author on reasonable request.

Acknowledgements

Methods

Protein expression and purification. The full-length (2-915) *Danio rerio* (zebrafish) TRPC4$_{DR}$ (NM_001289881) was cloned into the pEG BacMam vector (Goehring et al., 2014), with a C-terminal HRV-3C cleavage site followed by EGFP Twin-StrepII-tag® (WSHPQFEKGGGSGGGSGGGSAWSHPQFEK) and a N-terminal eight poly-histidine tag followed by a TEV cleavage site. Bacmid and baculovirus were produced as described previously (Goehring et al., 2014). In brief, P2 baculovirus produced in Sf9 cells, was added to HEK293 GnTI⁻ cells (mycoplasma test negative, ATCC #CRL-3022) grown in suspension in FreeStyle medium (GIBCO-Life Technologies #12338-018) supplemented with 2% FBS at 37 °C and 8% CO_2. Eight hours after transduction, 5 mM sodium butyrate was added to enhance protein expression for additional forty hours and the temperature was reduced to 30 °C. After 48 hours post-transduction, cells were harvested by low-speed centrifugation in an Avanti J-20 XP centrifuge (Beckman Coulter) at 8,983g for 15 min, washed in phosphate-buffered saline (PBS) pH 7.4, and pelleted in an Allegra X-15R (Beckman Coulter) Centrifuge at 4,713g for 15 min. The cell pellet was resuspended and cells were lysed in an ice-cooled Microfluidizer® Mod. 110S (Microfluidics Corporation) in buffer A (PBS buffer pH 7.4, 1 mM Tris(2-carboxyethyl)phosphine (TCEP), 10% glycerol) and protease inhibitors (0.2 mM AEBSF, 0.1 µM aprotonin and 1 µM phosphoramidion); 50 ml was used per pellet obtained from 800 ml of HEK 293 cell culture. Subsequently, the lysate was centrifuged at 15,000g for 5 min, and the membranes were collected by ultracentrifugation in an Optima XPN-80 ultracentrifuge (Beckman Coulter) equipped with a Type 70 Ti Rotor at 164,700g for one hour. The membranes were then mechanically homogenized in buffer B (100 mM Tris-HCl pH 8, 150 mM NaCl, 1 mM TCEP, 10 % glycerol) and protease inhibitors, quick-frozen and stored at -80°C till further purification. Membranes were solubilized for 2 hours in buffer B supplemented with 1% DDM/0.1% CHS (Anatrace #D310-CH210). Insoluble material was removed by ultracentrifugation for 1 hour in a Beckman Coulter Type 70 Ti Rotor at 164,700g. The soluble membrane fraction was diluted 2-fold with buffer B to reduce the detergent concentration and slowly applied to a column packed with Strep-Tactin beads (IBA Lifesciences) by gravity flow (6-10 seconds/drop) at 4 °C. Next, the resin was washed with 5 column volumes of buffer B supplemented with 0.04 % DDM/0.004 % CHS solution, 0.02 mg ml⁻¹ soy polar lipids (Avanti #541602) dissolved in DDM and protease inhibitors. Bound protein was eluted seven times with 0.5 column volumes of buffer A with 4 mM d-desthiobiotin (Sigma), 0.026% DDM/0.0026% CHS, 0.02 mg ml⁻¹ soy polar lipids and 0.1 mM AEBSF protease inhibitor. The C-terminal EGFP tag was removed by incubating the eluted fractions with HRV-3C protease

11

overnight. The next day, the detergent was replaced with amphipols A8-35 (Anatrace #A835) by adding four times the total protein mass and incubating for 6 hours at 4 °C. Detergent removal was performed by adding Biobeads SM2 (BioRad # 1523920) pre-equilibrated in PBS to the protein solution at 15 mg ml^{-1} final concentration for 1 hour, then replaced with fresh Biobeads at 20 mg ml^{-1} for overnight incubation at 4 °C. Biobeads were removed using a Poly-Prep column (BioRad #7311550) and the solution was centrifuged at 20,000g for 10 minutes to remove any precipitate. The protein was concentrated with a 100 MWCO Amicon centrifugal filter unit (Millipore) and purified by size exclusion chromatography using a Superose 6 10/300 GL column (GE healthcare) equilibrated in buffer C (PBS pH 7.4, 1 mM TCEP). The peak corresponding to tetrameric TRPC4$_{DR}$ in amphipols was collected and concentrated up to 0.3 mg ml^{-1} for both negative stain and cryo-EM analysis.

EM data acquisition. Tetramer TRPC4$_{DR}$ integrity was evaluated by negative stain electron microscopy prior to cryo-EM grid preparation and image acquisition (Gatsogiannis et al., 2016). In brief, 4 μl of TRPC4$_{DR}$ in amphipols at a concentration of 0.02 mg ml^{-1} were applied onto a freshly glow-discharged copper grid (Agar Scientific; G400C) with an additional thin carbon layer. After an incubation of 45 s, the sample was blotted with Whatman no. 4 filter paper and stained with 0.75% uranyl formate. The images were recorded manually with a JEOL JEM-1400 TEM, operated at an acceleration voltage of 120 kV, and a 4,000 × 4,000 CMOS detector F416 (TVIPS) with a pixel size of 1.84 Å/pixel (Figure S2c-e). For cryo-EM, 3.5 μl of TRPC4$_{DR}$ at a concentration of 0.25 mg ml^{-1} were applied onto freshly glow-discharged holey carbon grids (Quantifoil grid (1.2/1.3) 300 mesh) blotted using 2.5 s blotting time, 1 s draining time, 0 blotting force with 100% humidity at 4 °C and vitrified in liquid ethane cooled by liquid nitrogen using a Vitrobot Mark III (FEI Company). The quality of the grids was screened with a JEOL JEM 3200 FSC electron microscope equipped with a field-emission gun and an in-column energy filter operated at an acceleration voltage of 200 kV. The grids were then stored in liquid nitrogen.

Electron microscopy and single particle cryo-EM data processing. A cryo-EM data set of TRPC4$_{DR}$ in amphipols was collected on a C$_s$-corrected TITAN KRIOS electron microscope (FEI), equipped with a high-brightness field-emission gun (XFEG) operated at an acceleration voltage of 300 kV. The images were acquired on a K2 summit direct electron detector (Gatan) operated in counting mode with a calibrated pixel size of 1.09 Å/pixel on the sample level with a post column GIF BioQuantum LS energy filter (Gatan) using a slit width of 20 eV. Two data

12

sets were collected. The first data set with a total of 2,020 images was collected with sixty frames (200 ms/frame) and an exposure of 12 seconds resulting in a total dose of ~69.0 e$^-$ Å^{-2}. A second data set with a total of 1,870 images was recorded to increase the number of particles with forty frames (300 ms/frame) and an exposure of 12 seconds resulting in a total dose of ~74.4 e$^-$ Å^{-2}. All images were collected automatically using EPU (FEI). Motion correction was performed using the MotionCor2 program (Zheng et al., 2017).

All image processing was performed with the SPHIRE software package (Moriya et al., 2017) (Figure S4). Motion-corrected sums without dose weighting were used to determine the defocus and astigmatism in CTER (Moriya et al., 2017). The defocus range of the selected images was 0.84 - 2.93 µm (Table S1). Images with low quality were removed using the graphical CTF assessment tool in SPHIRE (Moriya et al., 2017). Motion-corrected sums with dose weighting were used for all other image processing steps. 426,377 single particles were picked automatically using CrYOLO (Wagner et al., unpublished). The particles were windowed to a final box size of 224 × 224 pixels. Reference-free 2-D classification and cleaning of the data set was performed with the iterative stable alignment and clustering approach ISAC (Yang et al., 2012) in SPHIRE. ISAC was performed at a pixel size of 3.02 Å/pixel. The 'Beautify' tool of SPHIRE was then applied to obtain refined and sharpened 2-D class averages at the original pixel size, showing high-resolution features (Figure S3a). A subset of ~132,622 particles producing 2-D class averages and reconstructions with high-resolution features were then selected for further structure refinement. An initial model for the first 3-D refinement was generated from the ISAC class averages with RVIPER. All 3-D refinements and classifications were performed imposing C4 symmetry. The 'clean' data set after ISAC was then subjected to 3-D refinements in MERIDIEN with a mask including amphiphols (Moriya et al., 2017). The final half-maps were combined, a tight mask and a B factor of -130.0 Å^2 were applied using SPHIRE's PostRefiner tool. This resulted in a cryo-EM map with an average resolution of 3.6 Å, as estimated by the 'gold standard' FSC = 0.143 criterion between the two masked half-maps (Figure S3f). The estimated accuracy of rotation and translation during the last iteration of the 3-D refinement were estimated to be 0.9375° and 0.7 pixels, respectively. Local FSC calculation was performed using the 'Local Resolution' tool in SPHIRE. This analysis showed that the core of TRPC4$_{DR}$ was resolved up to 3.1 Å resolution, whereas the upper and peripheral part of the protein showed the lowest resolution ($\sim$ 4.5 - 5 Å) (Figure S3e). The final density was then locally filtered on the basis of the local resolution with the 'LocalFilter' utility in the SPHIRE software package. Details related to data processing are summarized in Table S1.

3-D clustering into six groups was performed using the RSORT3D tool of SPHIRE with a 3-D

focused binary mask including the C-terminal helix and the ankyrin repeats. The resulting volumes were refined with the 'local refinement mode' of MERIDIEN in SPHIRE. The SPHIRE 'PostRefiner' tool was used to determine the resolution of the locally refined volumes.

Model building, refinement and validation. Initially, we built a homology model of TRPC4$_{DR}$ with Modeller (Eswar et al., 2008), using the structures of NOMPC (PDB-ID: 5VKQ) and TRPV1(PDB-ID: 3J5Q) as templates. These are the homologs with the highest sequence identity and of which high-resolution structures have been determined. Since only the transmembrane domain could be built using this method we used Rosetta to complete the model. Gaps in the membrane domain were built using RosettaCM (Wang et al., 2015). The rest of the monomer was built *de novo* using several iterative runs of the fragment fitting protocol implemented in Rosetta (Wang et al., 2015). After this, loops still missing from the model were manually built in Coot (Emsley et al., 2010). We generated a tetramer model by fitting four copies of the monomer model into the cryo-EM density using Chimera (Pettersen et al., 2004). With the tetramer, we built 18 additional amino acids the N-terminal end of the protein using the enumerative sampling strategy in Rosetta (rosettaES) (Frenz et al., 2017), which could not be reliably built manually due to the quality of the density in this region. Final manual model building, including fitting of lipids, was done in Coot (Emsley et al., 2010). The full model was finally refined in Phenix (Adams et al., 2010) using the real space refinement protocol. The final model comprises residues 18 -753 with missing sequence in between 119-134, 173-186, 273-283, 320-323, 389,390, 649-651, 661-695, 728-730. Finally, we used Molprobity (Chen et al., 2010) to validate the overall geometry of the model, Phenix (Adams et al., 2010) to calculate the model-to-map correlation, and EMRinger (Barad et al., 2015) to validate the side chain geometry. The densities corresponding to annular lipids were modelled as phosphatidic acid lipid with a shorter lipid tail (PDB-ID 44E) and CHS (PDB-ID YO1). The geometric restraints for the refinement of both lipids were obtained by the eLBOW module in PHENIX (Adams et al., 2010). Figures were prepared in Chimera (Pettersen et al., 2004) and VMD (Humphrey et al., 1996). Structure-based sequence alignment was done using the Multiseq plug (Roberts et al., 2006) in VMD. Multiple sequence alignment was done using Clustal Omega (Sievers et al., 2011). Figures of the sequence alignment were made with Jalview (Waterhouse et al., 2009). The radius of the pore was determined using HOLE (Smart et al., 1996). The pK$_a$ values of protein residues were calculated using the H++ server (Anandakrishnan et al., 2012) and used to assign the right protonation states in the calculation of electrostatic potentials in Chimera.

Electrophysiological recordings on HEK293 cells heterologously expressing TRPC4$_{DR}$-EGFP. HEK293 cells (ATCC, CRL-1573^{TM}, Manassas, USA) were cultured at 37 °C and 5% CO_2 in DMEM (Sigma, St. Louis, USA) supplemented with 10% fetal calf serum (Sigma, St. Louis, USA), and 5 % penicillin/streptomycin (Sigma, St. Louis, USA). One day prior to transient transfections the HEK293 cells were seeded on 24-well plates. The transient transfections of the seeded HEK293 cells with pCDNA3.1 carrying TRPC4$_{DR}$-EGFP using Lipofectamine 2000 (Invitrogen, Carlsbad, USA) were performed two days prior to the patch-clamp measurements.

Whole cell patch-clamp experiments on HEK293 cells heterologously expressing TRPC4$_{DR}$-EGFP were performed under voltage clamp conditions using the Axopatch 200B amplifier (Axon Instruments, Union City, USA) and the DigiData 1322A interface (Axon Instruments, Union City, USA). Patch pipettes with resistances of 2-5 mΩ were fabricated from thin-walled borosilicate glass on a horizontal puller (Model P-1000, Sutter Instruments, Novato, USA). The series resistance was <10 MΩ. The bath solution (Akbulut et al., 2015) contained 135 mM NaCl, 5 mM KCl, 1.2 mM $MgCl_2$, 1.5 mM $CaCl_2$, 8 mM glucose, 10 mM HEPES (pH titrated to 7.4 using NaOH) and the pipette solution contained 145 mM CsCl, 2 mM $MgCl_2$, 10 mM HEPES, 1 mM EGTA (sodium salt), 0.1 mM GTP (sodium salt, pH titrated to 7.2 with CsOH). For the recordings of the IV-curves the membrane potentials were clamped to values ranging from -90 mV to +90 mV. The measurements were conducted in the absence and in the presence of 50 nM (-)-Englerin A.
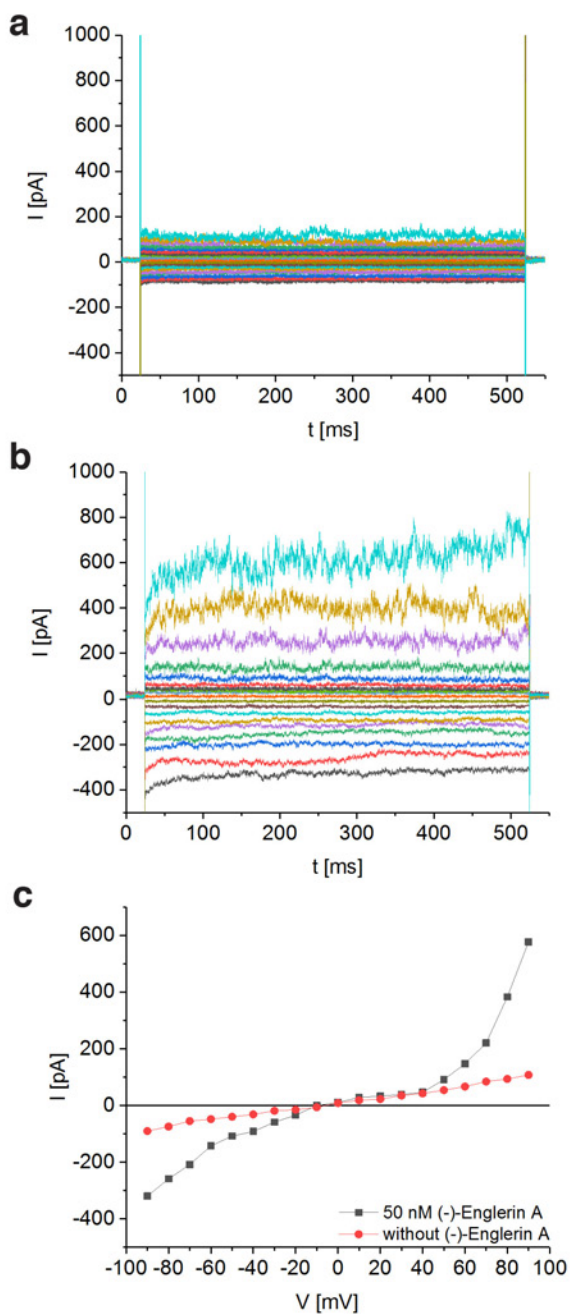
Figures

Figure 1. Activation of TRPC4$_{DR}$ by the selective activator (-)-Englerin A. a-b) HEK293 cells heterologously expressing TRPC4$_{DR}$-EGFP were investigated by voltage clamp experiments in the whole-cell configuration. The membrane potentials were clamped to values ranging from -90 mV to +90 mV in the absence **(a)** and in the presence **(b)** of 50 nM (-)-Englerin A. Upon addition of 50 nM (-)-Englerin A, the current density at -60 mV increased from -3.1 ± 1.9 pA/pF (n=6) to -16.7 ± 10.7 pA/pF (n=6). In untransfected control cells, the current density in the absence and presence of the activator was virtually the same with values of -2.1 ± 1.2 pA/pF (V = - 60 mV, n=5) and -1.8 ± 0.9 pA/pF (V = -60 mV, n=5) respectively. **c)** Current-voltage curves of the current traces depicted in **(a)** and **(b)**. Shown are typical recordings, which were measured on the same cell (typical of n = 6). The measurements were performed as described in Methods.
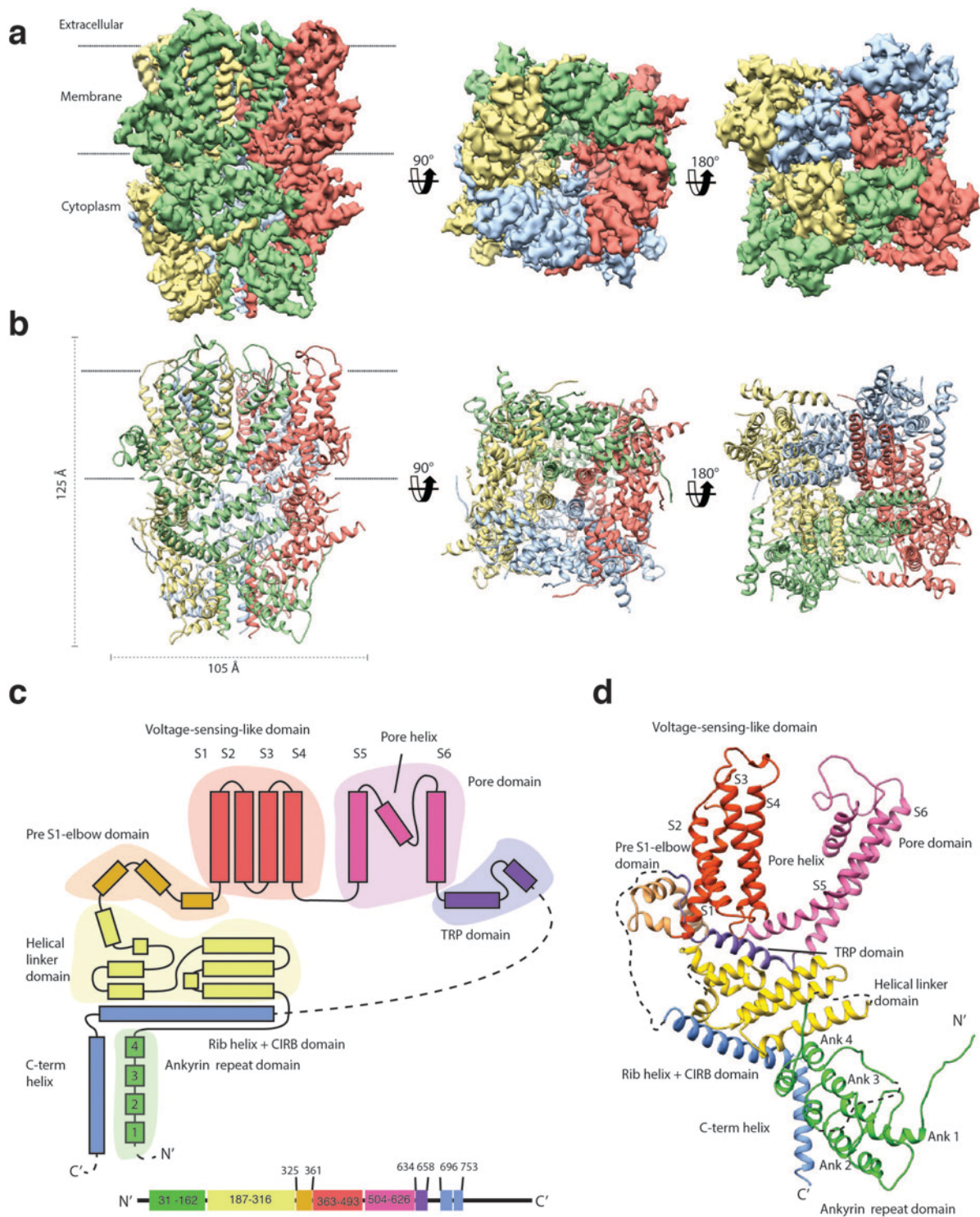
Figure 2. Structure of TRPC4$_{DR}$. a) Cryo-EM density map of TRPC4$_{DR}$ with each protomer colored differently and shown as side, top and bottom view. **b)** Ribbon representation of the atomic model of TRPC4$_{DR}$. Colors are the same as in **(a)**. **c)** Topology diagram depicting the domain organization of a TRPC4$_{DR}$ protomer. **d)** Ribbon representation of a TRPC4$_{DR}$ protomer. Each domain is shown in a different color and labeled accordingly.
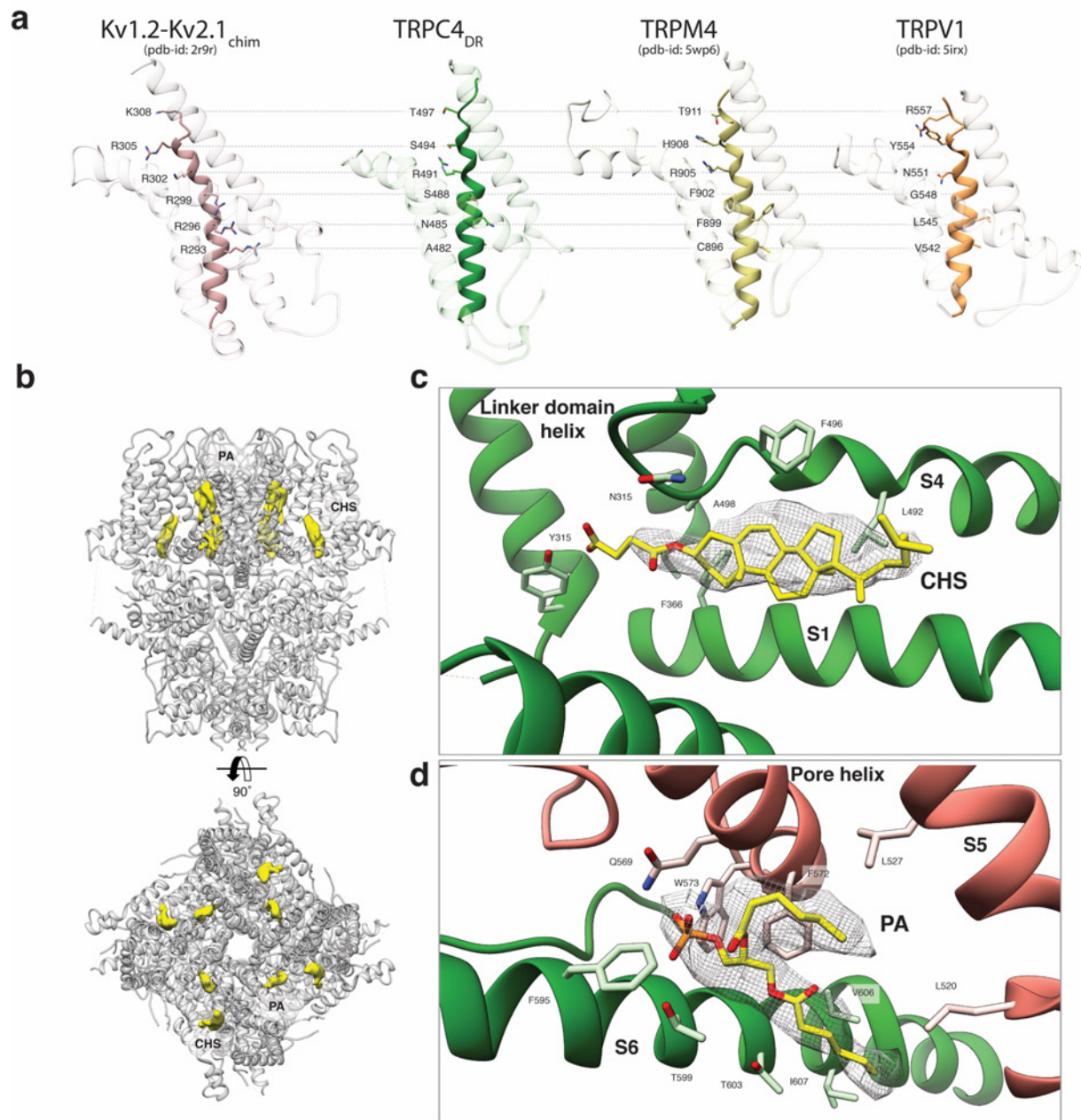
17

Figure 3. VSL domain and lipid binding sites. a) Comparison of the VSL domain of selected TRP family members with the voltage-sensing domain of the chimeric $K_V1.2-K_V2.1$ channel. The voltage-sensing domain of the chimeric $K_V1.2-K_V2.1$ channel and the VSL domains of TRPC4$_{DR}$,TRPM4, and TRPV1 are shown in ribbon representation. The S4 helix in each case is highlighted with dark shaded color. The rest of the domains are shown in light grey color. The residues important for voltage sensing in the S4 helix of the chimeric $K_V1.2-K_V2.1$ channel and homologous residues in the TRP channels are shown in stick representation and labeled. **b)** Lipid binding sites in the TRPC4$_{DR}$ structure. Side and top view of the TRPC4$_{DR}$ structure with lipid densities highlighted in yellow against the model shown in ribbon representation. **c-d)** Zoomed-in view on the cholesteryl hemisuccinate (CHS) and phosphatidic acid lipid (PA) binding sites, respectively. CHS and PA molecules are shown in yellow stick representation.
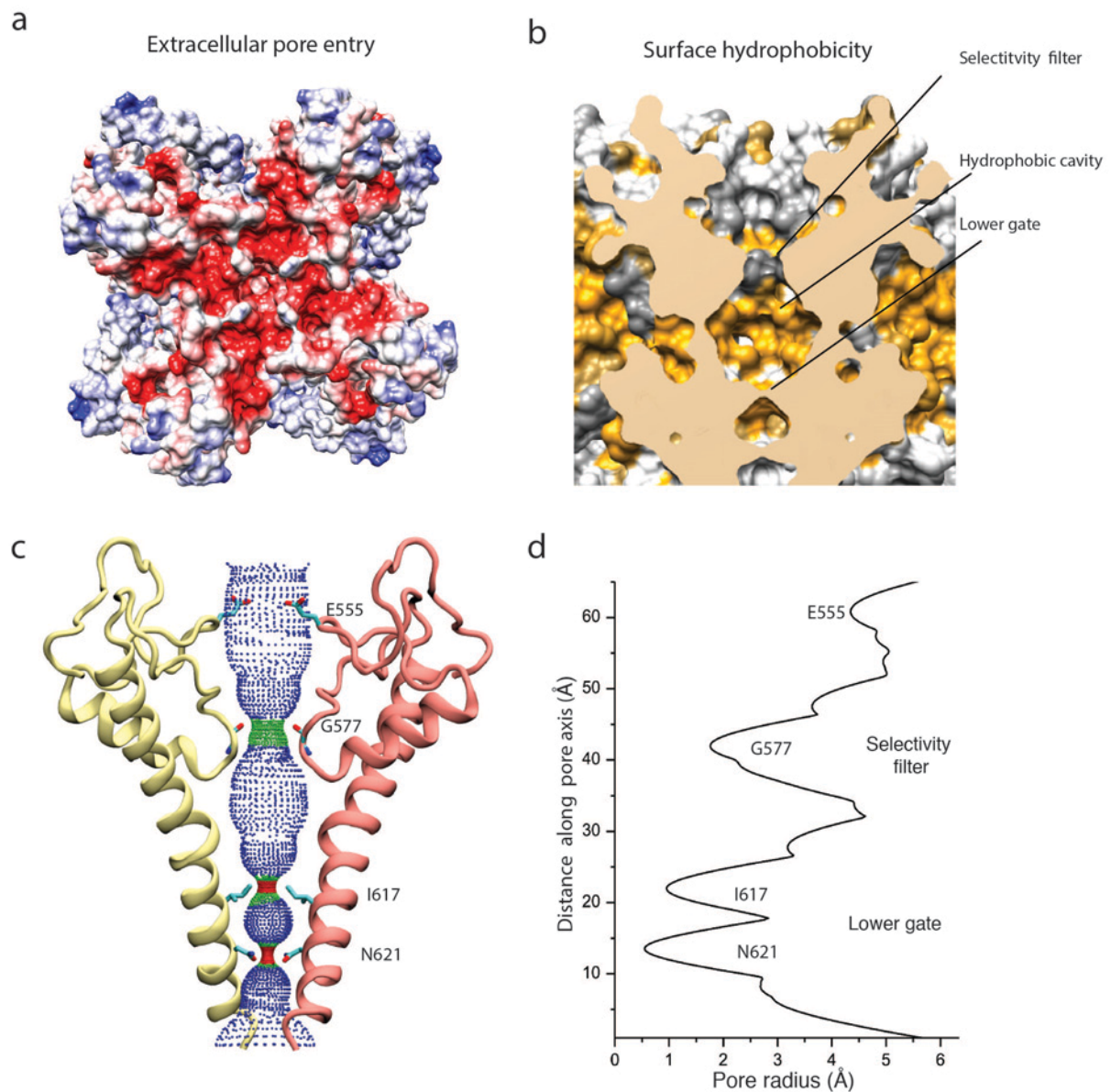
Figure 4. Architecture of the pore domain. a) Surface electrostatic Coulomb potential at the extracellular mouth of TRPC4$_{DR}$. **b**) Hydrophobic surface of the pore shown in vertical cross section. Hydrophobic patches are colored orange. **c**) Ion conduction pore of TRPC4$_{DR}$ shown with diagonally facing protomers shown in ribbon representation. Critical residues important for gating and selection are shown in stick representation. **d**) Pore radius determined along the pore axis using HOLE (Smart et al., 1996).
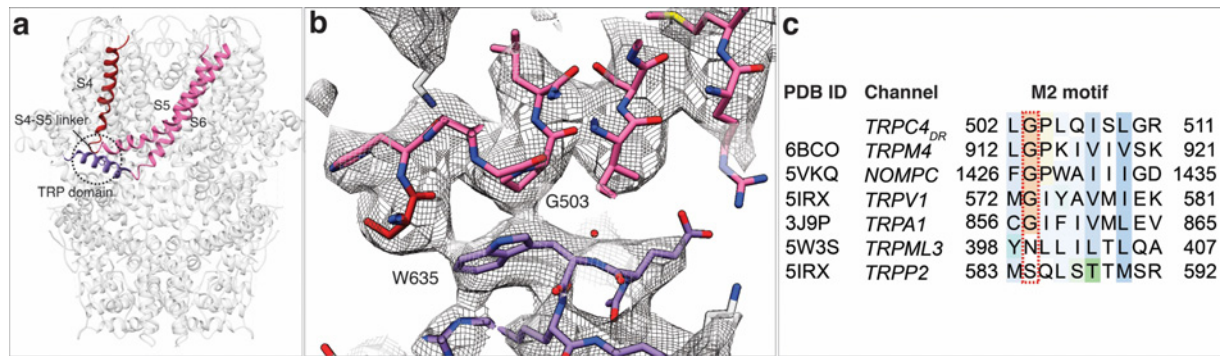
Figure 5. Interaction of the TRP domain with a conserved glycine in the S4-S5 linker. a) Ribbon overview indicating the interaction site between the TRP domain and the S4-S5 linker. Key helices are shown in different colors. The rest of the protein is shown in light grey. **b**) Zoomed-in view on the interaction site with key residues labeled. The chain trace is shown in stick representation. **c**) Structure-based sequence alignment of TRP family members. The conserved glycine in the M2 motif is highlighted by a red dotted box.
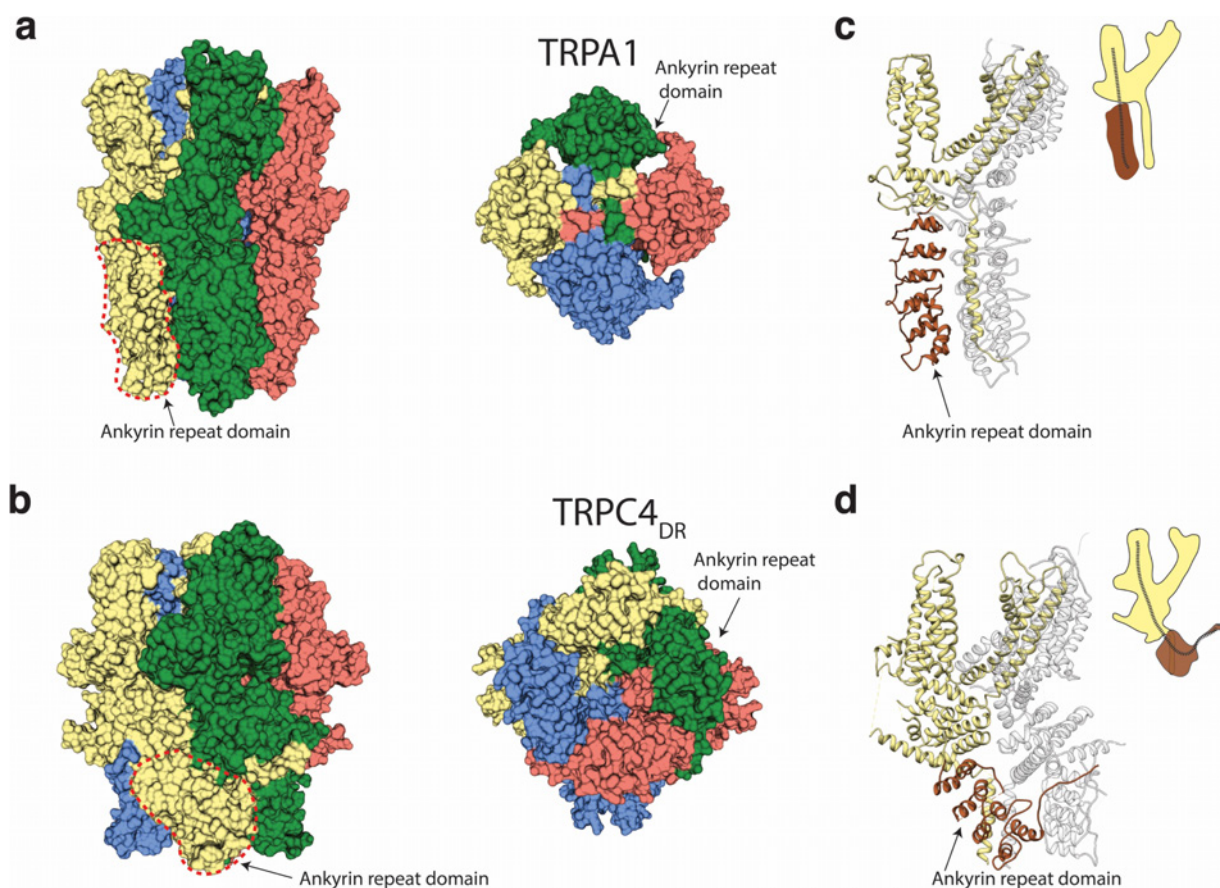

Figure 6. Comparison of the ankyrin domain arrangement of TRPC4$_{DR}$ and TRPA1. a-b) Side and top view of the structures of TRPA1 (PDB-ID: 3J9P) (**a**) and TRPC4$_{DR}$ (**b**) in surface representation. Each subunit is colored with unique colors. **c-d**) Ribbon and cartoon representation of TRPA1 (**c**) and TRPC4$_{DR}$ (**d**) showing two protomers in side view. The ankyrin repeats of one protomer are highlighted in brown.
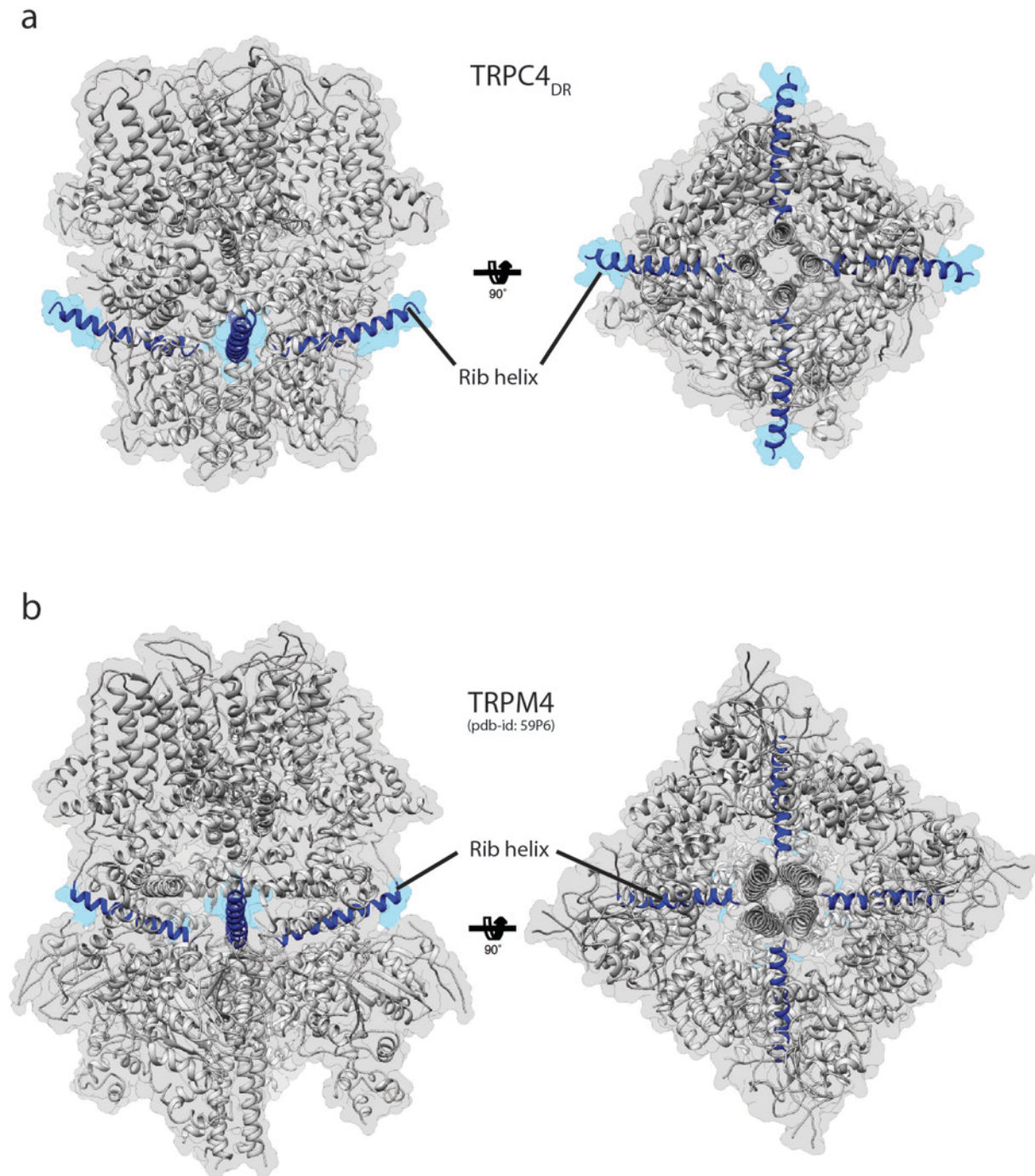
20

Figure 7. Position of the Rib helix in TRPC4$_{DR}$ and TRPM4. a-b) Side and top view of the atomic models of TRPC4$_{DR}$ (**a**), and TRPM4 (**b**). The Rib helix is highlighted in blue color and the density of the map is shown in the background with high transparency.
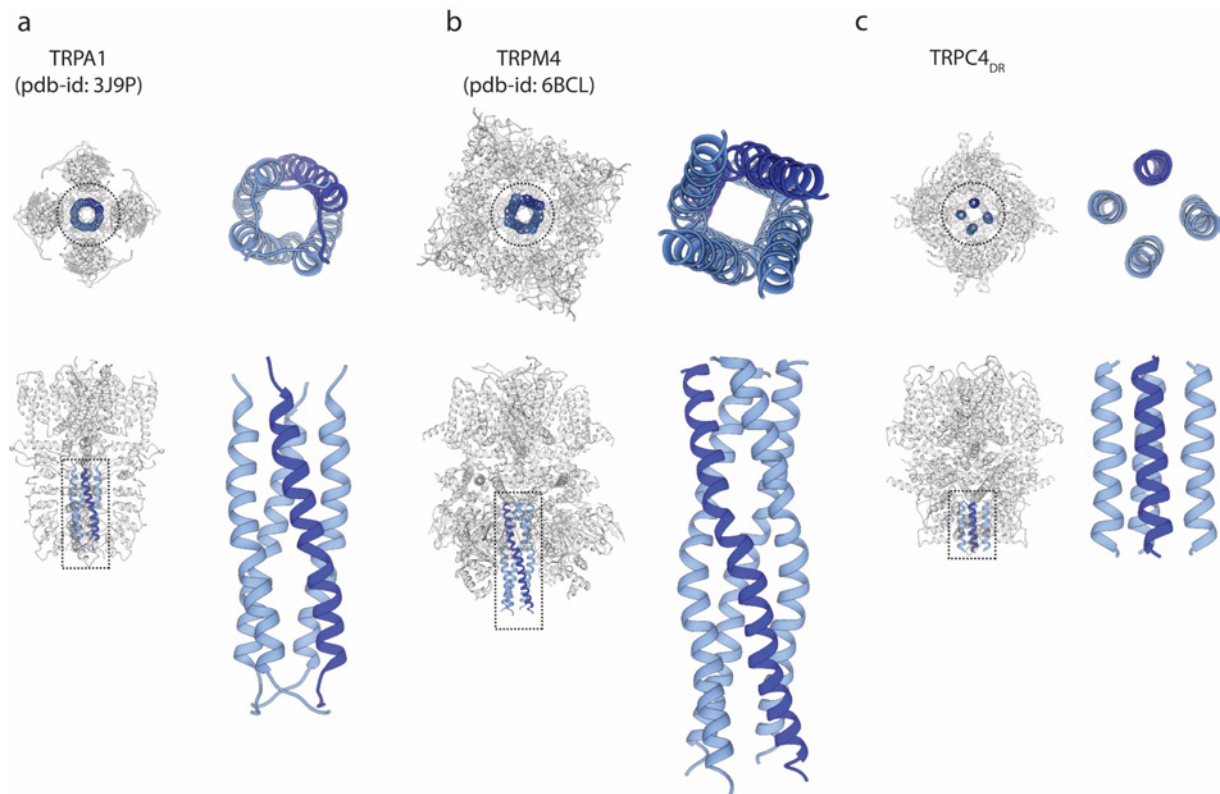
Figure 8. Comparison of the C-terminal helix architecture in TRPA1, TRPM4 and TRPC4DR. a-c) Each panel shows the complete tetramer in top and side view on the left and the zoomed-in view of the C-terminal helix alone in top and side view on the right. The C-terminal helix is shown in blue with one helix highlighted in shaded dark blue.

TRP family name	Residue	van der Waals diameter (Å)	Selectivity[1] PCa : PNa	Reference
TRPC4$_{DR}$	G577	3.7	7	
TRPV1	G643	1.5	3.8-9.6	(Cao et al., 2013)
TRPV2	Gly604 (M606)	1.9 (1.35)	3	(Zubcevic et al., 2016)
TRPML3	G457 (D459)	2.0 (4.2)	Highly selective for Ca^{2+}	(Zhou et al., 2017)
TRPML1	G470 (D471)	1.4 (2.1)	N.D.	(Schmiege et al., 2017)
TRPN (NOMPC)	G1506	3.8	N.D.	(Jin et al., 2017b)
TRPA1	D915	3.2	0.8	(Paulsen et al., 2015)
TRPV5	D542	2.6	>100	(Hughes et al., 2018)
TRPV6	D541	0.9	>100	(Saotome et al., 2016)
TRPM4	G972	4.3	PNa : PCa >100	(Guo et al., 2017)
TRPP2 (PKD2)	Leu641 (Gly642)	1.7 (3.6)	PNa : PCa >100	(Shen et al., 2016b)

[1] (Venkatachalam and Montell, 2007)

Table 1: Comparison of selectivity filters among TRP family members

23

Figure S1. Multiple sequence alignment of TRPC4$_{DR}$, human TRPC4 and human TRPC5.
The grey shaded regions highlight conserved residues. Helices are indicated by red bars.
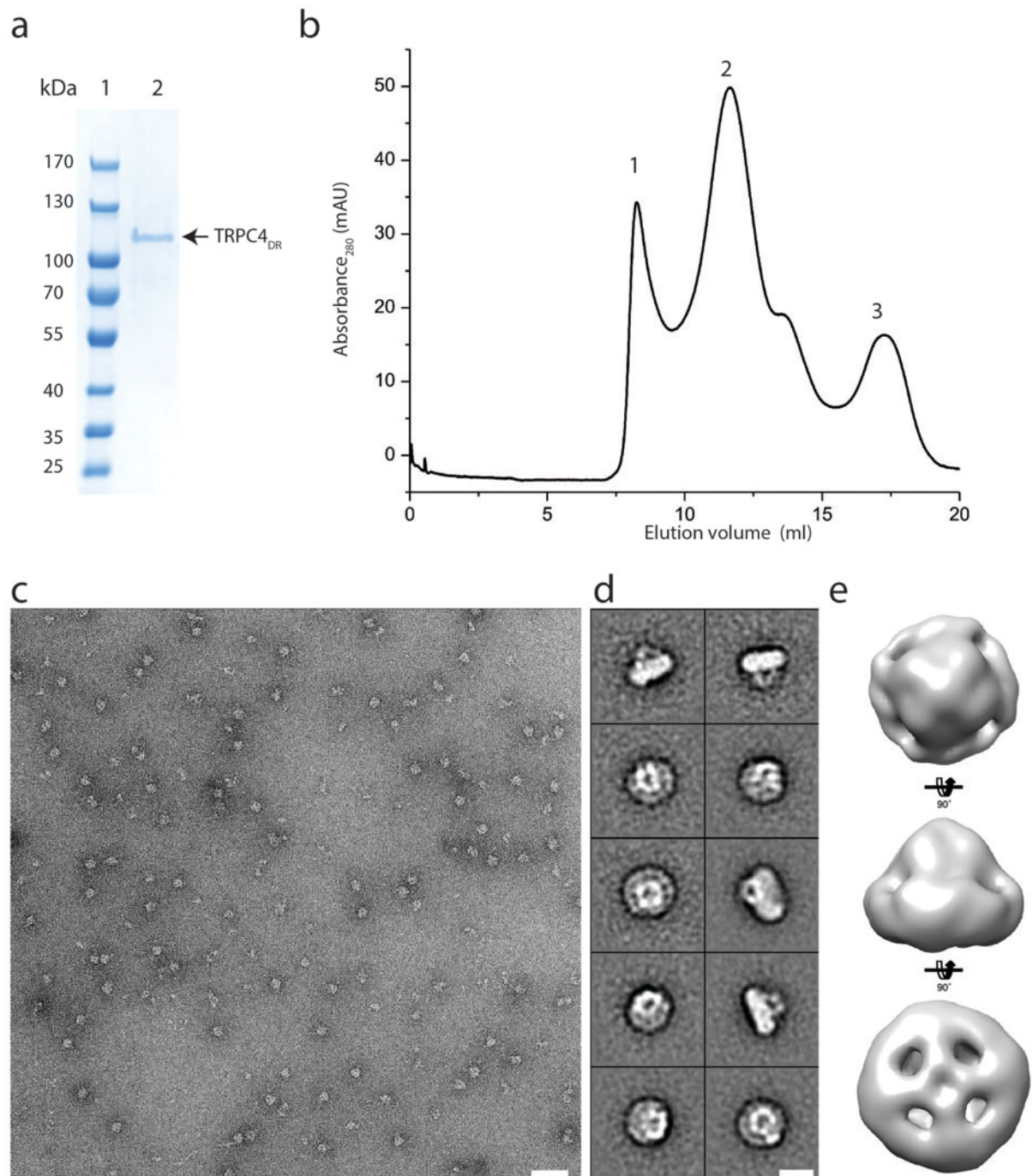
Figure S2. Purification of TRPC4$_{DR}$ and negative stain EM of TRPC4$_{DR}$ in amphipols. a) SDS-PAGE of the peak fraction of TRPC4$_{DR}$ in amphipols after size exclusion chromatography. Lane 1: molecular weight marker, lane 2: protein. **b**) Size exclusion chromatography profile of TRPC4$_{DR}$ in amphipols. Peak 1,2 and 3 correspond to the void volume, tetrameric TRPC4$_{DR}$ and cleaved GFP, respectively. **c**) Representative negative stain electron micrograph of TRPC4$_{DR}$. Scale bar, 50 nm, **d**) Representative 2-D class averages. Scale bar, 10 nm. **e**) 3-D reconstruction of negatively stained TRPC4$_{DR}$ shown in different orientations.
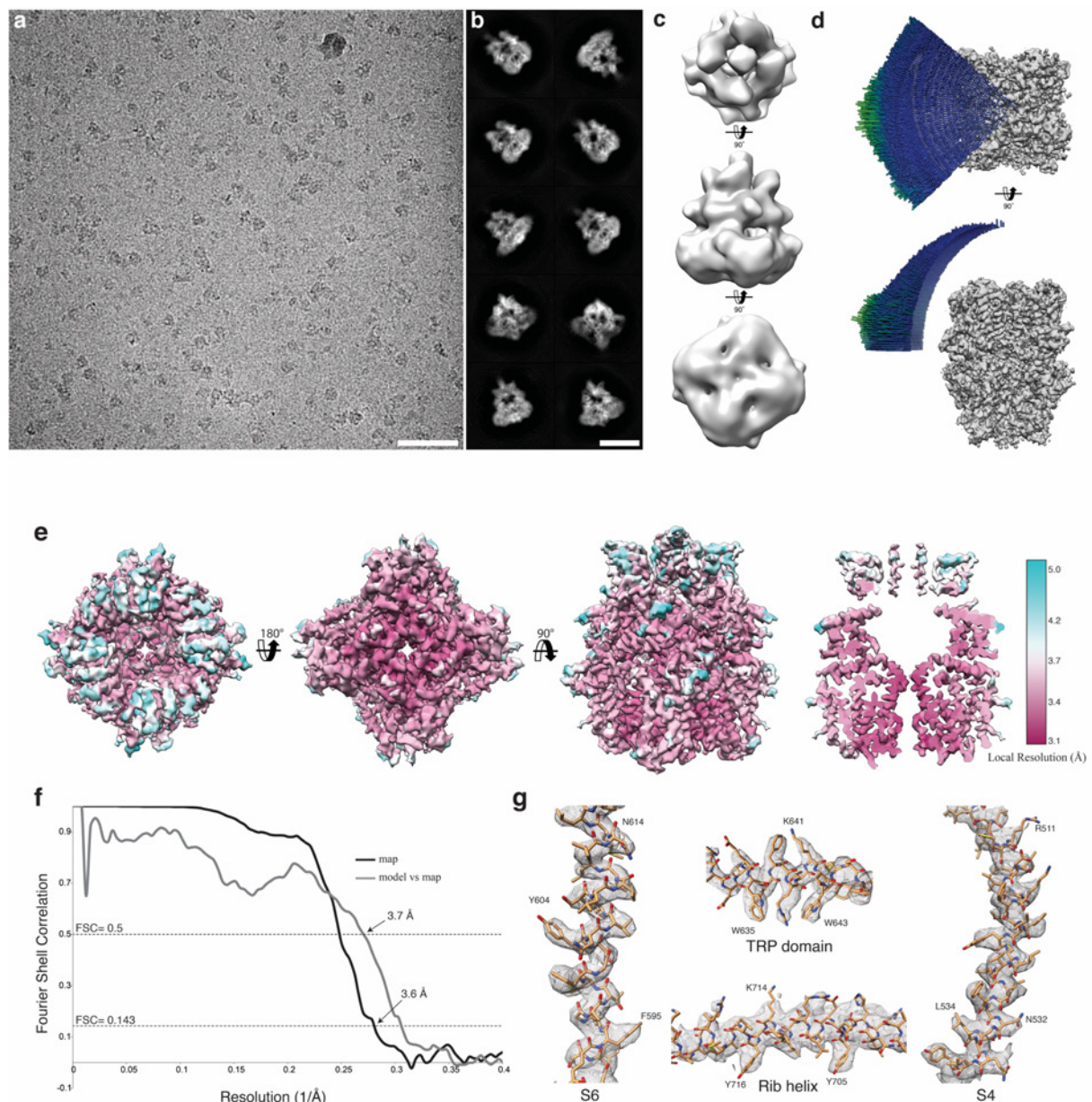
Figure S3. Cryo-EM structure of TRPC4$_{DR}$. a-b) Representative digital micrograph area (**a**) and selected 2-D class averages (**b**) of TRPC4$_{DR}$ embedded in vitrified ice. Scale bars, 50 nm (**a**), and 10 nm (**b**). **c**) The *ab initio* 3-D reconstruction obtained with RVIPER. **d**) Angular distribution of the particles. **e**) The cryo-EM density map of TRPC4$_{DR}$ colored according to the local resolution. **f**) Fourier Shell Correlation (FSC) curve between maps from two independently refined half data sets (black). The 0.143 criterion indicates an average resolution of 3.6 Å. The grey curve shows the FSC curve between the final map versus the atomic model. **g**) Representative regions of the density with fitted atomic model.
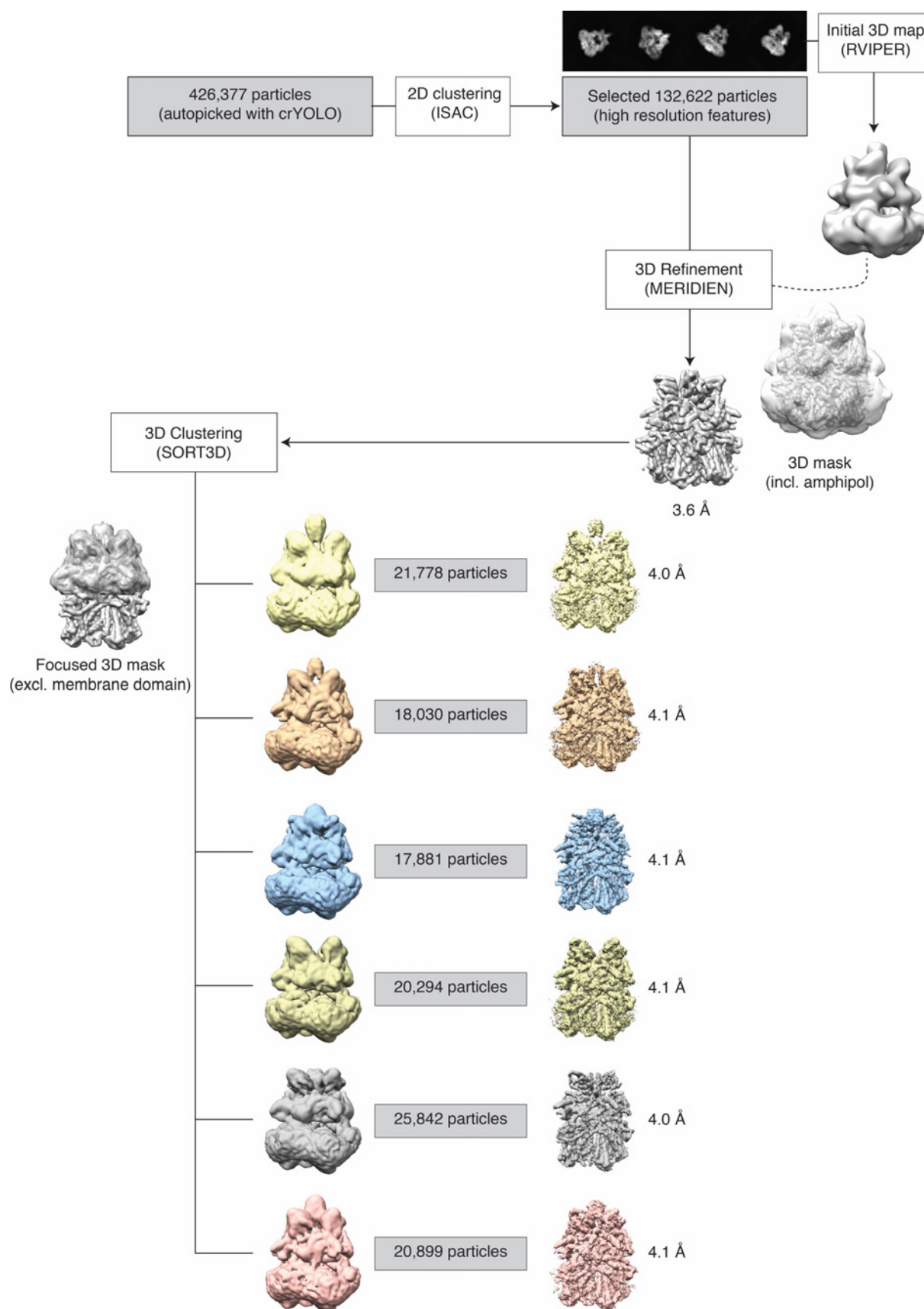
26

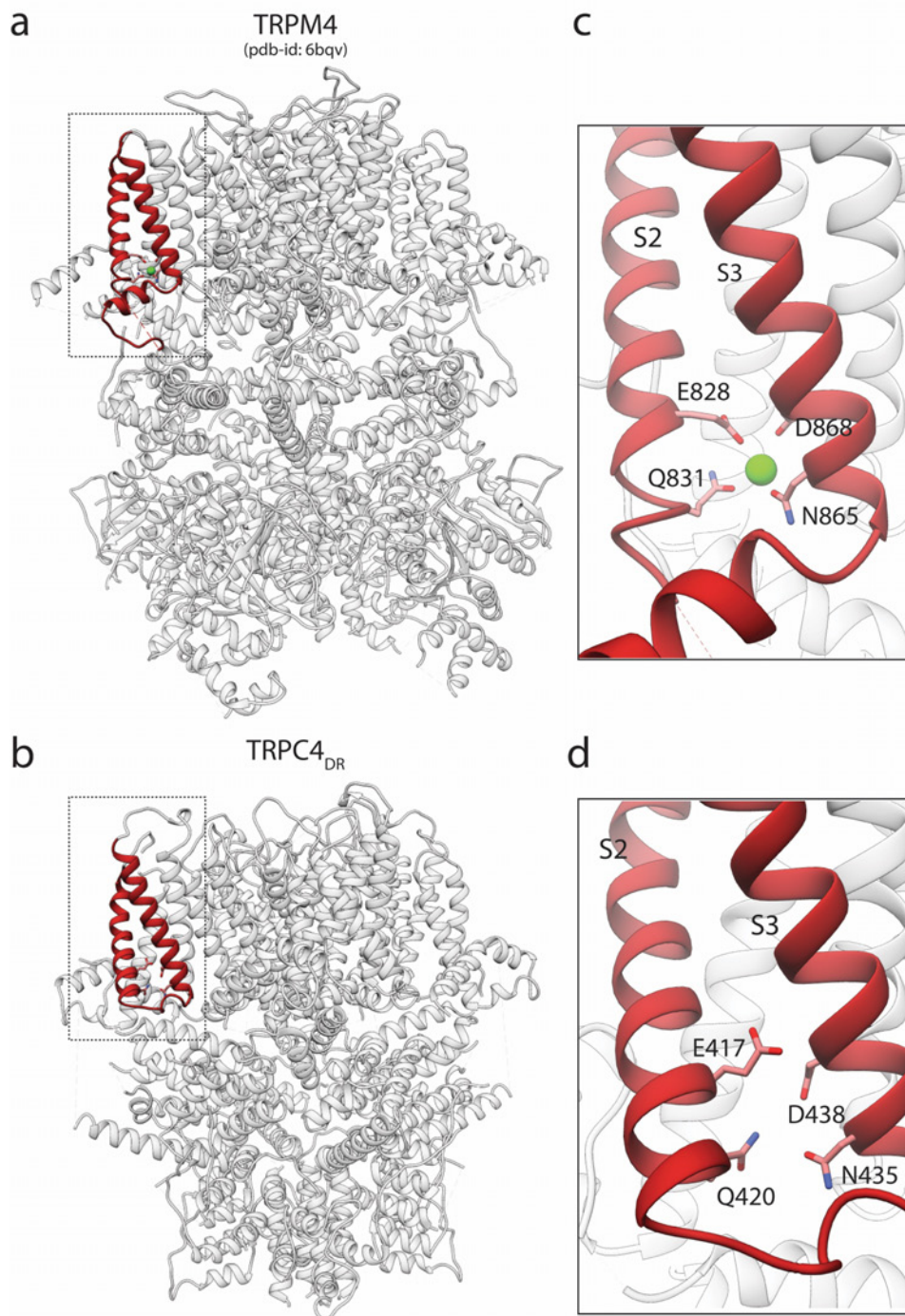**Figure S4. Single particle processing workflow for TRPC4$_{DR}$ structure determination.**

Figure S5. Comparison of the Ca^{2+} binding site in TRPM4 and TRPC4$_{DR}$. a-b) Side view of TRPM4 (**a**) and TRPC4$_{DR}$ (**b**) shown in ribbon representation. Helices involved in Ca^{2+}-binding are shown in red. Zoomed-in view on the Ca^{2+}-binding site in TRPM4 (**c**) and TRPC4$_{DR}$ (**d**). Residues involved in Ca^{2+} binding in TRPM4 and its topologically equivalent residues in TRPC4$_{DR}$ are shown in stick representation. Ca^{2+} ion is shown as green sphere.
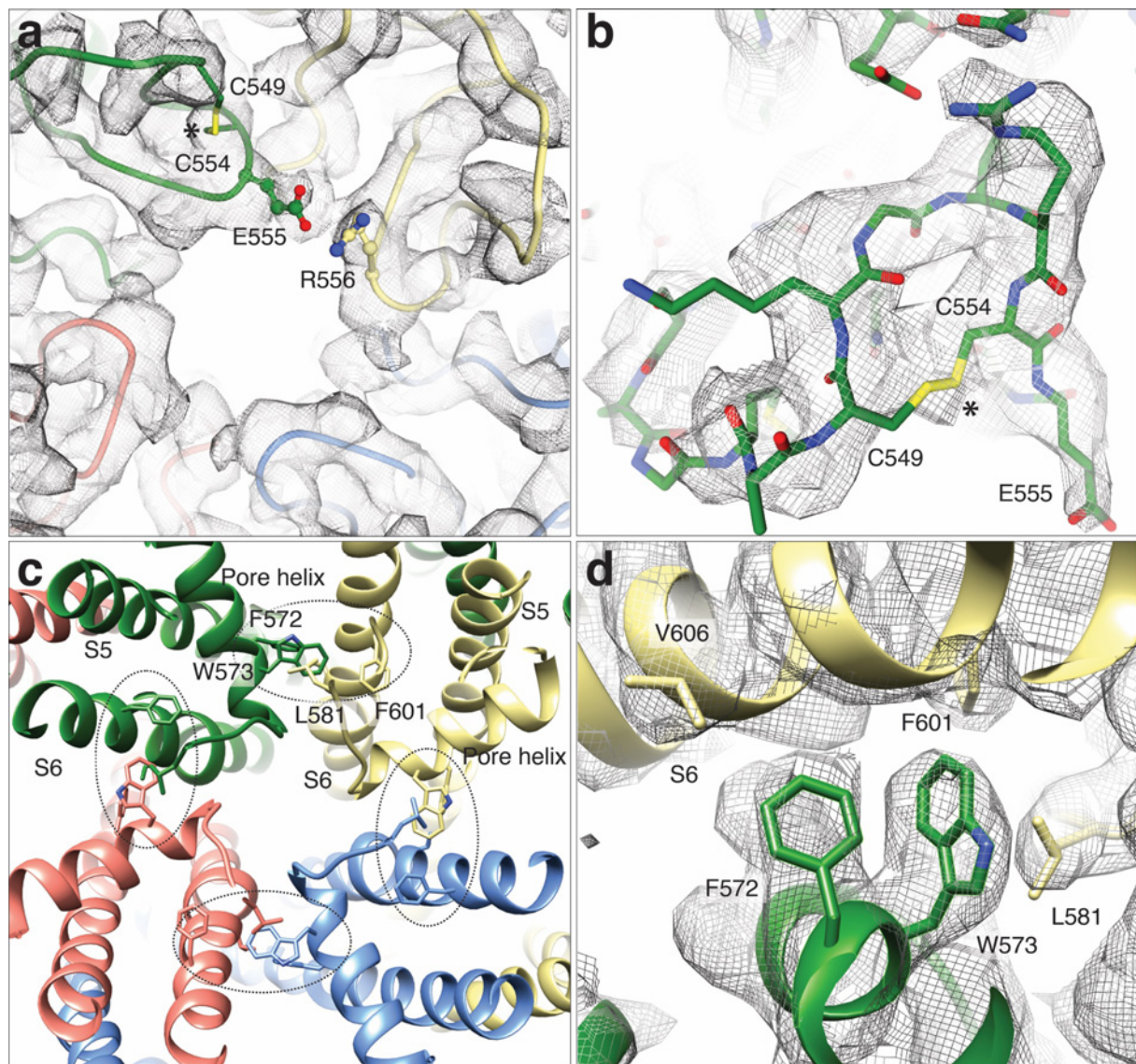
Figure S6. **LFW motif of the pore region and cysteines involved in disulphide bridges in the TRPC4DR structure. a**) Extracellular view near the pore axis showing the loops harboring cysteine residues. The loops are shown in ribbon representation with cysteines shown in stick representation. The neighboring glutamate residue is involved in an electrostatic interaction with an arginine. **b**) Zoomed-in view on the disulphide bridge region. The chain trace is shown in stick representation including the side chains. The disulphide bridge is indicated by an asterisk. Electron density in (**a**) and (**b**) is shown in wired grey mesh. **c**) LFW motif region viewed along the pore axis from the extracellular side. Each protomer is colored differently. The LFW motif and interacting residues are shown in stick representation. The interface at the LFW motif is highlighted with a black dotted ellipse. **d**) Zoomed-in view on the interface at the LFW motif. The density is shown in wired grey mesh with key residues highlighted.
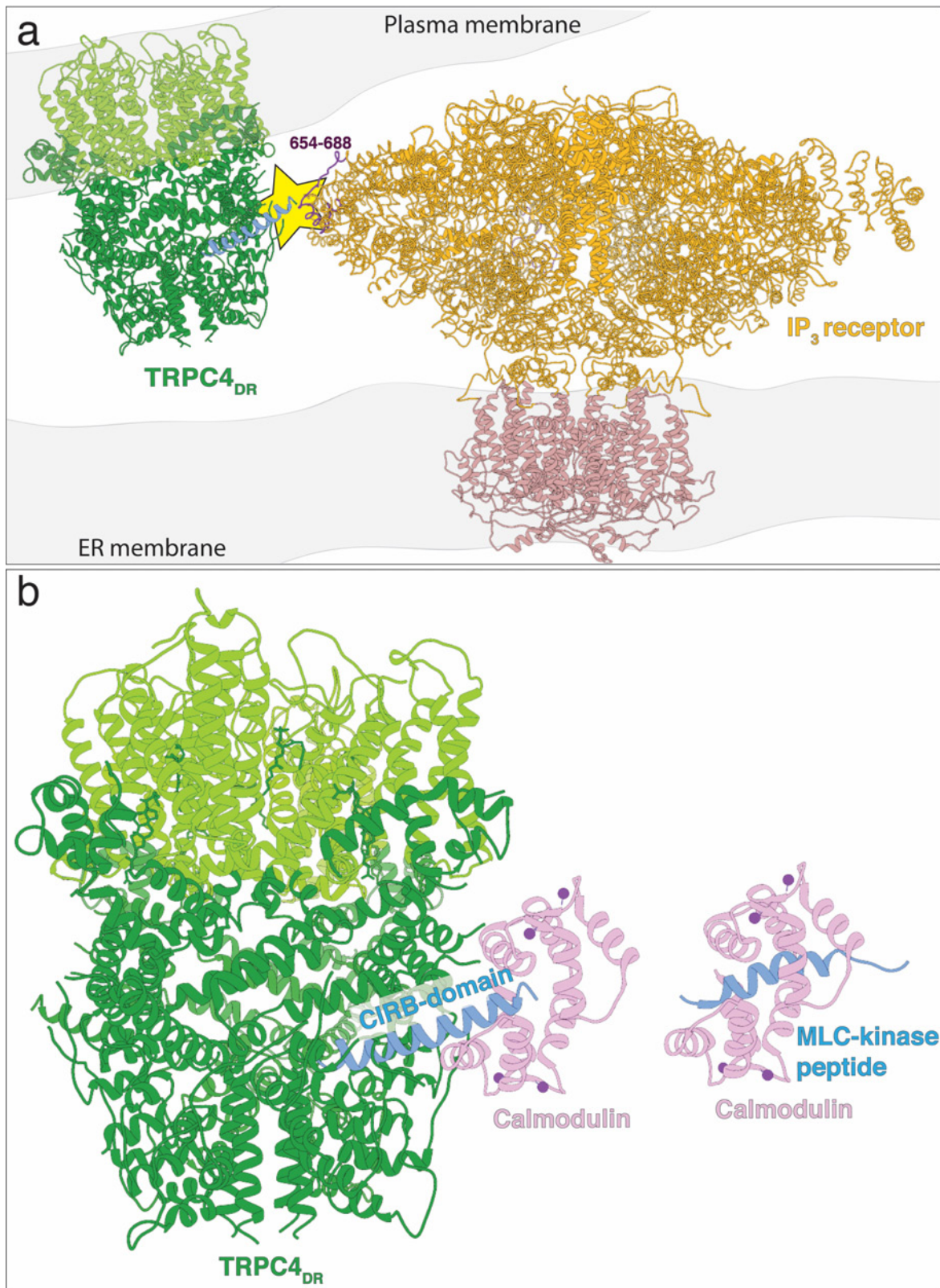
29

Figure S7. Predicted model of TRPC4$_{DR}$ interaction with IP$_3$ receptors and calmodulin. a) Possible interaction of an IP$_3$ receptor with TRPC4$_{DR}$. The putative site of interaction is highlighted with a yellow star. The CIRB domain of TRPC4$_{DR}$ is shown in blue. The predicted interacting region of the IP$_3$ receptor is highlighted in dark color. **b)** Interaction of calmodulin with the CIRB domain of TRPC4$_{DR}$. Calmodulin is shown in pink. Calcium is shown as spheres. Calmodulin has been fitted to the structure of TRPC4$_{DR}$ in analogy to the MLC-kinase peptide bound to calmodulin in the crystal structure (PDB-ID: 2LV6).

Data collection	Data set 1	Data set 2
Microscope	Titan Krios (Cs corrected, XFEG)	
Voltage (kV)	300	
Camera	K2 summit (Gatan)	
Pixel size (Å)	1.09	1.09
Number of frames	60	40
Total electron dose (e$^-$/Å^2)	69	74
Number of particles	132,622	
Estimated Defocus range	0.844 - 2.931	
Atomic model composition		
Non-hydrogen atoms	21,412	
Protein atoms	21,192	
Ligand atoms	236	
Refinement (Phenix)		
RMSD bond	0.01	
RMSD angle	1.11	
Model to map fit, CC mask	0.80	
Resolution (FSC@0.143, Å)	3.6	
Map sharpening B-factor (Å^2)	-130.0	
Validation		
Clashscore	3.53	
Poor rotamers (%)	0.17	
Favored rotamers (%)	94.48	
Ramachandran outliers (%)	0.0	
Ramachandran favored (%)	92.38	
Molprobity score	1.62	
EMRinger score	2.42	

Table S1. EM Data collection and refinement statistics of TRPC4$_{DR}$

Movie S1. Overview of the TRPC4$_{DR}$ structure

Movie S2. Morph between conformational states of TRPC4$_{DR}$

References

Adams, P.D., Afonine, P.V., Bunkóczi, G., Chen, V.B., Davis, I.W., Echols, N., Headd, J.J., Hung, L.-W., Kapral, G.J., Grosse Kunstleve, R.W., et al. (2010). PHENIX: a comprehensive Python-based system for macromolecular structure solution. Acta Crystallogr. D Biol. Crystallogr. *66*, 213–221.

Akbulut, Y., Gaunt, H.J., Muraki, K., Ludlow, M.J., Amer, M.S., Bruns, A., Vasudev, N.S., Radtke, L., Willot, M., Hahn, S., et al. (2015). (-)-Englerin A is a potent and selective activator of TRPC4 and TRPC5 calcium channels. Angew. Chem. Int. Ed. Engl. *54*, 3787–3791.

Anandakrishnan, R., Aguilar, B., and Onufriev, A.V. (2012). H++ 3.0: automating pK prediction and the preparation of biomolecular structures for atomistic molecular modeling and simulations. Nucleic Acids Res. *40*, W537–W541.

Autzen, H.E., Myasnikov, A.G., Campbell, M.G., Asarnow, D., Julius, D., and Cheng, Y. (2018). Structure of the human TRPM4 ion channel in a lipid nanodisc. Science *359*, 228–232.

Barad, B.A., Echols, N., Wang, R.Y.-R., Cheng, Y., DiMaio, F., Adams, P.D., and Fraser, J.S. (2015). EMRinger: side chain-directed model and map validation for 3D cryo-electron microscopy. Nat Meth *12*, 943–946.

Beck, A., Speicher, T., Stoerger, C., Sell, T., Dettmer, V., Jusoh, S.A., Abdulmughni, A., Cavalié, A., Philipp, S.E., Zhu, M.X., et al. (2013). Conserved gating elements in TRPC4 and TRPC5 channels. Journal of Biological Chemistry *288*, 19471–19483.

Cao, E., Liao, M., Cheng, Y., and Julius, D. (2013). TRPV1 structures in distinct conformations reveal activation mechanisms. Nature *504*, 113–118.

Chen, Q., She, J., Zeng, W., Guo, J., Xu, H., Bai, X.-C., and Jiang, Y. (2017). Structure of mammalian endolysosomal TRPML1 channel in nanodiscs. Nature 1–17.

Chen, V.B., Arendall, W.B., Headd, J.J., Keedy, D.A., Immormino, R.M., Kapral, G.J., Murray, L.W., Richardson, J.S., and Richardson, D.C. (2010). MolProbity: all-atom structure validation for macromolecular crystallography. Acta Crystallogr. D Biol. Crystallogr. *66*, 12–21.

Emsley, P., Lohkamp, B., Scott, W.G., and Cowtan, K. (2010). Features and development of Coot. Acta Crystallogr. D Biol. Crystallogr. *66*, 486–501.

Eswar, N., Eramian, D., Webb, B., Shen, M.-Y., and Sali, A. (2008). Protein structure modeling with MODELLER. Methods Mol. Biol. *426*, 145–159.

Flockerzi, V. (2007). An introduction on TRP channels. Handb Exp Pharmacol 1–19.

Freichel, M., Tsvilovskyy, V., and Camacho-Londoño, J.E. (2014). TRPC4- and TRPC4-Containing Channels. In The Actin Cytoskeleton, B.M. Jockusch, ed. (Berlin, Heidelberg: Springer Berlin Heidelberg), pp. 85–128.

Frenz, B., Walls, A.C., Egelman, E.H., Veesler, D., and DiMaio, F. (2017). RosettaES: a sampling strategy enabling automated interpretation of difficult cryo-EM maps. Nat Meth *14*, 797–800.

Gao, Y., Cao, E., Julius, D., and Cheng, Y. (2016). TRPV1 structures in nanodiscs reveal mechanisms of ligand and lipid action. Nature *534*, 347–351.

Gatsogiannis, C., Merino, F., Prumbaum, D., Roderer, D., Leidreiter, F., Meusch, D., and Raunser, S. (2016). Membrane insertion of a Tc toxin in near-atomic detail. Nat Struct Mol Biol *23*, 884–890.

Goehring, A., Lee, C.-H., Wang, K.H., Michel, J.C., Claxton, D.P., Baconguis, I., Althoff, T., Fischer, S., Garcia, K.C., and Gouaux, E. (2014). Screening and large-scale expression of membrane proteins in mammalian cells for structural studies. Nat Protoc *9*, 2574–2585.

Guo, J., She, J., Zeng, W., Chen, Q., Bai, X.-C., and Jiang, Y. (2017). Structures of the calcium-activated, non-selective cation channel TRPM4. Nature *552*, 205–209.

Hannan, M.A., Kabbani, N., Paspalas, C.D., and Levenson, R. (2008). Interaction with dopamine D2 receptor enhances expression of transient receptor potential channel 1 at the cell surface. Biochim Biophys Acta *1778*, 974–982.

Hirschi, M., Herzik, M.A., Wie, J., Suo, Y., Borschel, W.F., Ren, D., Lander, G.C., and Lee, S.-Y. (2017). Cryo-electron microscopy structure of the lysosomal calcium-permeable channel TRPML3. Nature 1–20.

Hughes, T.E.T., Lodowski, D.T., Huynh, K.W., Yazici, A., Del Rosario, J., Kapoor, A., Basak, S., Samanta, A., Han, X., Chakrapani, S., et al. (2018). Structural basis of TRPV5 channel inhibition by econazole revealed by cryo-EM. Nat Struct Mol Biol *25*, 53–60.

Humphrey, W., Dalke, A., and Schulten, K. (1996). VMD: visual molecular dynamics. J Mol Graph *14*, 33–8–27–8.

Jeon, J.-P., Hong, C., Park, E.J., Jeon, J.-H., Cho, N.-H., Kim, I.-G., Choe, H., Muallem, S., Kim, H.J., and So, I. (2012). Selective Gαi subunits as novel direct activators of transient receptor potential canonical (TRPC)4 and TRPC5 channels. Journal of Biological Chemistry *287*, 17029–17039.

Jin, P., Bulkley, D., Guo, Y., Zhang, W., Guo, Z., Huynh, W., Wu, S., Meltzer, S., Cheng, T., Jan, L.Y., et al. (2017a). Electron cryo-microscopy structure of the mechanotransduction channel NOMPC. Nature *547*, 118–122.

Jin, P., Bulkley, D., Guo, Y., Zhang, W., Guo, Z., Huynh, W., Wu, S., Meltzer, S., Cheng, T., Jan, L.Y., et al. (2017b). Electron cryo-microscopy structure of the mechanotransduction channel NOMPC. Nature *547*, 118–122.

Kühlbrandt, W. (2014). The Resolution Revolution. Science *343*, 1443–1444.

Lee, K.P., Yuan, J.P., So, I., Worley, P.F., and Muallem, S. (2010). STIM1-dependent and STIM1-independent function of transient receptor potential canonical (TRPC) channels tunes their store-operated mode. Journal of Biological Chemistry *285*, 38666–38673.

Liao, M., Cao, E., Julius, D., and Cheng, Y. (2013). Structure of the TRPV1 ion channel determined by electron cryo-microscopy. Nature *504*, 107–112.

Lin, Z., Chen, Q., Lee, M., Cao, X., Zhang, J., Ma, D., Chen, L., Hu, X., Wang, H., Wang, X., et al. (2012). Exome sequencing reveals mutations in TRPV3 as a cause of Olmsted syndrome. Am. J. Hum. Genet. *90*, 558–564.

Liu, X., Singh, B.B., and Ambudkar, I.S. (2003). TRPC1 is required for functional store-operated Ca2+ channels. Role of acidic amino acid residues in the S5-S6 region. J Biol Chem *278*, 11337–11343.

Long, S.B., Tao, X., Campbell, E.B., and MacKinnon, R. (2007). Atomic structure of a voltage-dependent K+ channel in a lipid membrane-like environment. Nature *450*, 376–382.

Madej, M.G., and Ziegler, C.M. (2018). Dawning of a new era in TRP channel structural biology by cryo-electron microscopy. 1–13.

McGoldrick, L.L., Singh, A.K., Saotome, K., Yelshanskaya, M.V., Twomey, E.C., Grassucci, R.A., and Sobolevsky, A.I. (2018). Opening of the human epithelial calcium channel TRPV6. Nature *553*, 233–237.

Mery, L., Magnino, F., Schmidt, K., Krause, K.H., and Dufour, J.F. (2001). Alternative splice variants of hTrp4 differentially interact with the C-terminal portion of the inositol 1,4,5-trisphosphate receptors. FEBS Lett *487*, 377–383.

Mery, L., Strauss, B., Dufour, J.F., Krause, K.H., and Hoth, M. (2002). The PDZ-interacting domain of TRPC4 controls its localization and surface expression in HEK293 cells. Journal of Cell Science *115*, 3497–3508.

Miehe, S., Bieberstein, A., Arnould, I., Ihdene, O., Rütten, H., and Strübing, C. (2010). The phospholipid-binding protein SESTD1 is a novel regulator of the transient receptor potential channels TRPC4 and TRPC5. Journal of Biological Chemistry *285*, 12426–12434.

Montell, C. (2005). The TRP superfamily of cation channels. Sci. STKE *2005*, re3.

Moriya, T., Saur, M., Stabrin, M., Merino, F., Voicu, H., Huang, Z., Penczek, P.A., Raunser, S., and Gatsogiannis, C. (2017). High-resolution Single Particle Analysis from Electron Cryo-microscopy Images Using SPHIRE. J Vis Exp e55448–e55448.

Nilius, B., and Flockerzi, V. (2014). Mammalian transient receptor potential (TRP) cation channels. Preface. Handb Exp Pharmacol *223*, v–vi.

Odell, A.F., Van Helden, D.F., and Scott, J.L. (2008). The spectrin cytoskeleton influences the surface expression and activation of human transient receptor potential channel 4 channels. J Biol Chem *283*, 4395–4407.

Okada, T., Shimizu, S., Wakamori, M., Maeda, A., Kurosaki, T., Takada, N., Imoto, K., and Mori, Y. (1998). Molecular cloning and functional characterization of a novel receptor-activated TRP Ca2+ channel from mouse brain. J Biol Chem *273*, 10279–10287.

Owsianik, G., Talavera, K., Voets, T., and Nilius, B. (2006). Permeation and selectivity of TRP channels. Annu. Rev. Physiol. *68*, 685–717.

Paulsen, C.E., Armache, J.-P., Gao, Y., Cheng, Y., and Julius, D. (2015). Structure of the TRPA1 ion channel suggests regulatory mechanisms. Nature *520*, 511–517.

Pettersen, E.F., Goddard, T.D., Huang, C.C., Couch, G.S., Greenblatt, D.M., Meng, E.C., and Ferrin, T.E. (2004). UCSF Chimera--a visualization system for exploratory research and analysis. J Comput Chem *25*, 1605–1612.

Plant, T.D., and Schaefer, M. (2003). TRPC4 and TRPC5: receptor-operated Ca2+-permeable nonselective cation channels. Cell Calcium *33*, 441–450.

Roberts, E., Eargle, J., Wright, D., and Luthey-Schulten, Z. (2006). MultiSeq: unifying sequence and structure data for evolutionary analysis. BMC Bioinformatics *7*, 382.

Saotome, K., Singh, A.K., Yelshanskaya, M.V., and Sobolevsky, A.I. (2016). Crystal structure of the epithelial calcium channel TRPV6. Nature *534*, 506–511.

Schaefer, M., Plant, T.D., Obukhov, A.G., Hofmann, T., Gudermann, T., and Schultz, G. (2000). Receptor-mediated regulation of the nonselective cation channels TRPC4 and TRPC5. J Biol Chem *275*, 17517–17526.

Schaefer, M., Plant, T.D., Stresow, N., Albrecht, N., and Schultz, G. (2002). Functional differences between TRPC4 splice variants. J Biol Chem *277*, 3752–3759.

Schindl, R., Frischauf, I., Kahr, H., Fritsch, R., Krenn, M., Derndl, A., Vales, E., Muik, M., Derler, I., Groschner, K., et al. (2008). The first ankyrin-like repeat is the minimum indispensable key structure for functional assembly of homo- and heteromeric TRPC4/TRPC5 channels. Cell Calcium *43*, 260–269.

Schmiege, P., Fine, M., Blobel, G., and Li, X. (2017). Human TRPML1 channel structures in open and closed conformations. Nature 1–16.

Sedgwick, S.G., and Smerdon, S.J. (1999). The ankyrin repeat: a diversity of interactions on a common structural framework. Trends Biochem Sci *24*, 311–316.

Shen, P.S., Yang, X., DeCaen, P.G., Liu, X., Bulkley, D., Clapham, D.E., and Cao, E. (2016a). The Structure of the Polycystic Kidney Disease Channel PKD2 in Lipid Nanodiscs. Cell *167*, 763–767.e11.

Shen, P.S., Yang, X., DeCaen, P.G., Liu, X., Bulkley, D., Clapham, D.E., and Cao, E. (2016b). The Structure of the Polycystic Kidney Disease Channel PKD2 in Lipid Nanodiscs. Cell *167*, 763–773.e11.

Sievers, F., Wilm, A., Dineen, D., Gibson, T.J., Karplus, K., Li, W., Lopez, R., McWilliam, H., Remmert, M., Söding, J., et al. (2011). Fast, scalable generation of high-quality protein multiple sequence alignments using Clustal Omega. Mol. Syst. Biol. *7*, 539.

Smart, O.S., Neduvelil, J.G., Wang, X., Wallace, B.A., and Sansom, M.S. (1996). HOLE: a program for the analysis of the pore dimensions of ion channel structural models. J Mol Graph *14*, 354–60–376.

Strübing, C., Krapivinsky, G., Krapivinsky, L., and Clapham, D.E. (2003). Formation of novel TRPC channels by complex subunit interactions in embryonic brain. J Biol Chem *278*, 39014–39019.

Swartz, K.J. (2008). Sensing voltage across lipid membranes. Nature *456*, 891–897.

Tang, J., Lin, Y., Zhang, Z., Tikunova, S., Birnbaumer, L., and Zhu, M.X. (2001). Identification of common binding sites for calmodulin and inositol 1,4,5-trisphosphate receptors on the carboxyl termini of trp channels. J Biol Chem *276*, 21303–21310.

Trost, C., Bergs, C., Himmerkus, N., and Flockerzi, V. (2001). The transient receptor potential, TRP4, cation channel is a novel member of the family of calmodulin binding proteins. Biochemical Journal *355*, 663–670.

Venkatachalam, K., and Montell, C. (2007). TRP channels. Annu Rev Biochem *76*, 387–417.

Wang, R.Y.-R., Kudryashev, M., Li, X., Egelman, E.H., Basler, M., Cheng, Y., Baker, D., and DiMaio, F. (2015). De novo protein structure determination from near-atomic-resolution cryo-EM maps. Nat Meth *12*, 335–338.

Waterhouse, A.M., Procter, J.B., Martin, D.M.A., Clamp, M., and Barton, G.J. (2009). Jalview Version 2--a multiple sequence alignment editor and analysis workbench. Bioinformatics *25*, 1189–1191.

Winkler, P.A., Huang, Y., Sun, W., Du, J., and Lü, W. (2017). Electron cryo-microscopy structure of a human TRPM4 channel. Nature *552*, 200–204.

Wu, D., Huang, W., Richardson, P.M., Priestley, J.V., and Liu, M. (2008). TRPC4 in rat dorsal root ganglion neurons is increased after nerve injury and is necessary for neurite outgrowth. J Biol Chem *283*, 416–426.

Wu, X., Eder, P., Chang, B., and Molkentin, J.D. (2010). TRPC channels are necessary mediators of pathologic cardiac hypertrophy. Proceedings of the National Academy of Sciences *107*, 7000–7005.

Yang, Z., Fang, J., Chittuluru, J., Asturias, F.J., and Penczek, P.A. (2012). Iterative stable alignment and clustering of 2D transmission electron microscope images. Structure *20*, 237–247.

Yin, Y., Wu, M., Zubcevic, L., Borschel, W.F., Lander, G.C., and Lee, S.-Y. (2018). Structure of the cold- and menthol-sensing ion channel TRPM8. Science *359*, 237–241.

Yoshida, T., Inoue, R., Morii, T., Takahashi, N., Yamamoto, S., Hara, Y., Tominaga, M., Shimizu, S., Sato, Y., and Mori, Y. (2006). Nitric oxide activates TRP channels by cysteine S-nitrosylation. Nat. Chem. Biol. *2*, 596–607.

Yuan, J.P., Kiselyov, K., Shin, D.M., Chen, J., Shcheynikov, N., Kang, S.H., Dehoff, M.H., Schwarz, M.K., Seeburg, P.H., Muallem, S., et al. (2003). Homer binds TRPC family channels and is required for gating of TRPC1 by IP3 receptors. Cell *114*, 777–789.

Zeng, W., Yuan, J.P., Kim, M.S., Choi, Y.J., Huang, G.N., Worley, P.F., and Muallem, S. (2008). STIM1 gates TRPC channels, but not Orai1, by electrostatic interaction. Molecular Cell *32*, 439–448.

Zheng, S.Q., Palovcak, E., Armache, J.-P., Verba, K.A., Cheng, Y., and Agard, D.A. (2017). MotionCor2: anisotropic correction of beam-induced motion for improved cryo-electron microscopy. Nat Meth *14*, 331–332.

Zhou, X., Li, M., Su, D., Jia, Q., Li, H., Li, X., and Yang, J. (2017). Cryo-EM structures of the human endolysosomal TRPML3 channel in three distinct states. Nat Struct Mol Biol *24*, 1146–1154.

Zhu, M.X. (2005). Multiple roles of calmodulin and other Ca(2+)-binding proteins in the functional regulation of TRP channels. Pflugers Arch - Eur J Physiol *451*, 105–115.

Zubcevic, L., Herzik, M.A., Jr, Ben C Chung, Liu, Z., Lander, G.C., and Lee, S.-Y. (2016). Cryo-electron microscopy structure of the TRPV2 ion channel. Nature Publishing Group *23*, 180–186.